Design of a Single Element 3D Ultrasound Scanner

by

Xiang Zhang

B.S. University of Maryland (2013)

Submitted to the Department of Mechanical Engineering
in partial fulfillment of the requirements for the degree of

Master of Science in Mechanical Engineering

at the

MASSACHUSETTS INSTITUTE OF TECHNOLOGY

June 2015

Author .....
Department of Mechanical Engineering
May 8, 2015

Certified by .....
Brian W. Anthony
Principal Research Scientist, Department of Mechanical Engineering
Thesis Supervisor

Accepted by .....
David E. Hardt
Graduate Officer, Department of Mechanical Engineering

Design of a Single Element 3D Ultrasound Scanner

by

Xiang Zhang

Submitted to the Department of Mechanical Engineering
on May 8, 2015, in partial fulfillment of the
requirements for the degree of
Master of Science in Mechanical Engineering

Abstract

Over the past decade, substantial effort has been directed toward developing ultrasonic systems for medical imaging. With advances in computational power, previously theorized scanning methods such as ultrasound tomography can now be realized. This thesis presents the design, error analysis, and initial image reconstructions from a single element 3D ultrasound tomography system. The system enables volumetric pulse echo or transmission imaging of distal limbs, for applications including: improving prosthetic fittings, monitoring bone density, and characterizing muscle health. The system is designed as a flexible mechanical platform for iterative development of algorithms targeting imaging of soft tissue with bone. The mechanical system independently controls movement of two single element ultrasound transducers in a cylindrical water tank. Each transducer can independently circle about the center of the tank as well as move vertically in depth. High resolution positioning feedback ($\sim 1\mu m$) and control enables flexible positioning of the transmitter and the receiver around the cylindrical tank; exchangeable transducers enable algorithm testing with varying transducer frequencies and beam geometries. High speed data acquisition (DAQ) through a dedicated National Instrument PXI setup streams digitized data directly to the host PC. System positioning error has been quantified and is within limits for the desired imaging modality. Imaging of various objects including: calibration objects, phantoms, bone, animal tissue, and human forearm are presented accordingly.

Thesis Supervisor: Brian W. Anthony
Title: Principal Research Scientist, Department of Mechanical Engineering

Acknowledgments

I would like to thank my advisor Brian Anthony for the continued guidance and support during this project. Brian's expansive set of knowledge helped guide me through the previously unfamiliar territories in this project. In addition, Brian always helped support the project needs in both hardware and software, but more importantly adding the right personnel to move the project forward.

I would also like to thank Jon Fincke, our resident acoustics expert. His understanding of acoustic imaging has helped push the project forward in both algorithm development and how to improve the mechanical design. His acoustic data processing skills and Matlab expertise has helped crunch much of the data I have produced.

I'd also like to thank Stephen Racca and the "Bench to Bucks" team for their concept generation and additional prototyping after completion of the class.

Contents

List of Figures

List of Tables

Chapter 1

Introduction

Ultrasound imaging has been used widely in the clinical setting for several decades. It is inherently safe and cost-effective, compared to other major imaging modalities such as X-ray, computed tomography (CT), and magnetic resonance imaging (MRI). Comparing the number of ultrasound procedures done globally in 2011 versus the number done in 2000, there has been more than an order of magnitude increase in quantity (250M $\rightarrow$ 2800M) [26]. Whereas, the number of MRI and CT scans only doubled (35M $\rightarrow$ 80M and 75M $\rightarrow$ 160M respectively). However, the number of digital X-ray procedures in 2011 (3300M) did surpass ultrasound [26]. This is likely due better penetration of X-rays through the body when compared to ultrasound. However, X-rays procedures expose patients to ionizing radiation and X-ray machines are generally costly and non-portable. With the increase in transistor density following Moore's Law and the miniaturization of electronic devices, ultrasound systems have evolved from bulky work stations to laptop sized portables. Additional ultrasound imaging modes such as doppler, 3D, and elastography, have also been enabled.

The image quality of ultrasound is typically lower than other modalities. Recent research into ultrasound tomography (UST) has mitigated this statement. The UST principle has been known since the 1970s [24], but only recently has computational power become sufficient to reconstruct images on clinically relevant time scales. UST systems incorporating ultrasound transmission and reflection data of the breast have produced images with qualities comparable to those of MRI [22] [11]. As seen in

Fig. 1-1a and Fig. 1-1b, UST images are almost indistinguishable from MRI images. Quantitative speed of sound and attenuation mapping of the breast with UST can also diagnose and localize tumors via differences in tissue density [21].

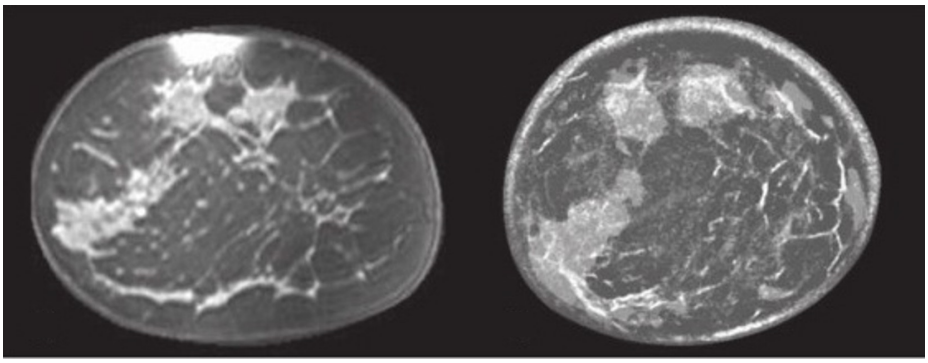

(a) Coronal breast MRI image (left). Compounded UST image (right) [22]

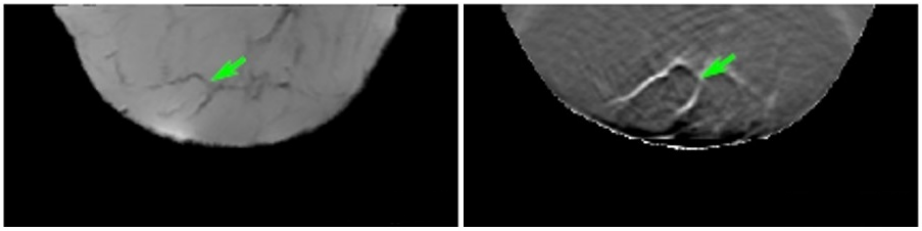

(b) Sagittal breast MRI image with image registration (left). Compounded UST image (right) [11]

Figure 1-1: Comparison of UST images to MRI images

Inspired from the UST results, we aim to utilize the UST technique for volumetric limb imaging. Unlike soft tissue imaging of the breast, limb imaging gives rise to complex propagation modes, mode conversion, and multiple paths due to the presence of bone. At typical medical ultrasound frequencies (1-5MHz), bones typically cause shadowing within the image. However, transmission of ultrasound is possible at lower frequencies (0.5-1MHz) and have been used classify patients with and without osteoporosis [13]. To develop a UST system for volumetric limb imaging, innovations in both hardware and software are necessary. Novel scanning systems are needed, including transducers, mechanical positioning structures and actuators, and data acquisition setups. The scanning system must be capable of recording both reflected and transmitted waves inside the appropriate scan volume. New algorithms account-

ing for the complex propagation of sound waves in bone are necessary to accurately reconstruct tomographic data. The developed hardware should be sufficiently flexible to support rapid and iterative development of various complex algorithms and support use of various transducers.

1.1 Clinical Motivation

Using ultrasound to image bone and the surrounding tissue results in strong refraction, attenuation, and scattering of the transmitted acoustic waves. Typical assumptions made in soft tissue imaging do not hold with the presence of bone. In this regard, scans of soft tissue with bone presents an interesting set of new imaging challenges and applications [14]. Accurate quantitative characterization of bone and surrounding soft tissues has wide potential in BLANK applications. We consider several motivating clinical needs: (1) improve prosthetic fittings by integrating internal tissue and bone structural information into the socket design process [4], (2) monitor bone density deterioration for osteoporosis progression and diagnosis [13], and (3) better quantify neuromuscular disease progression such as Duchenne's muscular dystrophy [6].

1.1.1 Prosthetic Fitting

The current plaster casting method for prosthetic fitting is a largely subjective process [16]. Typical fittings require several iteration to achieve a desirable fit. Improper fittings at the limb-socket interface can cause neuromas, inflammation, soft tissue calcifications, and pressure sores [16]. Any of these pain inducing pathologies can force the wearer into a wheelchair or crutches, reducing their mobility and quality of life. The prosthetics fitting challenge hinges on the ability to record skin and bone surfaces of adequately high-resolution. A 3D ultrasound system capable of accurately segmenting the skin surface and the bone surface, while being integrated into a prosthetic CAD modeling system will substantially improve the socket design process [27].

1.1.2 Bone Mineral Density Monitoring

Osteoporosis (a condition under which the bone mineral density (BMD) is substantially reduced) is a condition affecting a significant part (>50% in the US) of the population aged 50 and above [19]. Osteoporosis greatly increases the risk of fractures, which can be particularly debilitating at the older age. Early diagnosis, quantitative measurement, and monitoring are important to manage the progression of the condition, but also to assess the efficacy of new treatments. Currently, X-ray is the predominant imaging modality for such diagnosis and monitoring. However, it is estimated that one must lose ∼30% of BMD to be noted on X-rays [19]. A more sensitive testing modality could provide earlier osteoporosis diagnosis and improve BMD measurement accuracy. The clinical potential of ultrasound to study bone fractures was first explored for monitoring of fracture healing [12]. Variation in the transmission of ultrasound through the heel can be used to classify patients with and without osteoporosis [13]. Volumetric ultrasound imaging through a distal limb could be used to volumetrically map the speed of sound and attenuation inside the bone, providing a richer set of measurements of the bone mineral density.

1.1.3 Muscle Deterioration Monitoring

Characterized by progressive disability leading to death, Duchenne muscular dystrophy (DMD) remains one of the most common and devastating neuromuscular disorders of childhood [3]. It is caused by a genetic mutation which generates a complex sequence of events in muscle cells which eventually undergo fibrosis and are replaced by adipose and connective tissue. Average survival of DMD patients is to the age of 25, although in some cases patients have survived into their forties. Although a variety of promising new treatment strategies are in development, outcome measures for clinical trials remain limited for the most part to a set of functional measures, such as the six-minute walk test [6]. While clearly useful, such measures are impacted by unrelated factors, such as mood and effort, and have limited repeatability. To address this and other limitations, magnetic resonance imaging (MRI) is now being

investigated as a surrogate measure. However, more easily applicable, cost-effective, office-based surrogate measures that provide high repeatability and sensitivity while still correlating strongly to disease status would find wider use in Phase II and possibly in Phase III clinical trials in DMD. A 3D ultrasound system capable of providing quantitative measurements of the muscle deterioration can serve as a convenient, non-invasive, clinically meaningful method to track DMD disease progression that surpasses the functional measures currently in use.

1.2 Thesis Scope

This thesis describes the design of a 3D ultrasound imaging system capable of both reflective and transmission imaging of a limb. In Chapter 2 and 3, existing UST systems are first described and system requirements for volumetric tomographic imaging are extracted with reference to the defined clinical motivations. Detailed mechanical and electrical design and construction of the system is presented in Chapter 4 and 5, followed by system characterization in Chapter 6. Initial echo imaging and tomography scans on the completed system is presented in Chapter 7-9.

Chapter 2

Ultrasound Tomography

With the increase of computational power in the past decade, ultrasound tomography (UST) is emerging as a promising new imaging modality for imaging of soft tissues. Recent systems targeting in-vivo breast imaging have produced clinically relevant images with quality and resolution comparable to those of MRI [5], [11]. However, an UST system for in-vivo imaging and quantitative characterization of soft tissue surrounding bone has not yet been developed. For this thesis, we aim to design a system that supports *iterative development and testing of algorithms for ultrasound imaging of soft tissue with bone motivated by a few target clinical applications.*

2.1 Soft Tissue Ultrasound Tomography Systems

The kinematics of current UST enabled systems vary greatly to accommodate the respective transducer architectures. Transducer architectures include: ring arrays, conical arrays, array probes, and single elements. Advantages and disadvantages for each architecture will be evaluated in the following sections, with reference to designing a rapid algorithm development system to target the clinical motivations listed in Chapter 1.

2.1.1 Ring Arrays

Ring transducer systems typically consists of a rigid ring transducer (256-2048 elements) scanning in one axis along the target, reconstructing 2D slices of the object. Such systems were the first to provide clinically relevant data and obtain FDA approval [5]. The first Computed Ultrasound Risk Evaluation prototype (CURE) developed by Duric et al. used a $20cm$ diameter ring transducer consisting of 256 elements [5]. The system produced compounded breast ultrasound images of quality rivaling those of MRI [22]. A denser ring transducer ($15cm$ 2048 elements) system was designed by Waag and Fedewa, but has not been used for clinical imaging [28]. The two systems shown in Fig, 2-1 below, enable reflective imaging with attenuation and sound speed mapping within the circular aperture. Due to the high number of transducers, complex data acquisition (DAQ) hardware is necessary for parallel sampling of the numerous receive channels. Custom sampling and multiplexing hardware were developed for each scan system. Custom ring transducers are costly when compared to commercial hand held probes and are not easily exchangeable.

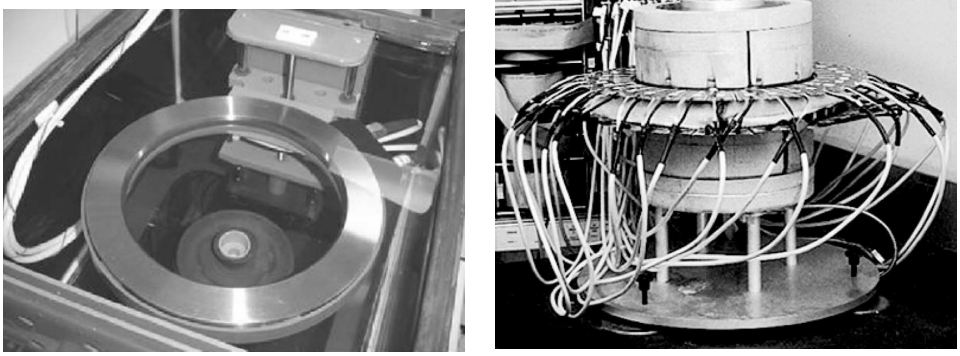

(a) CURE system by Duric et al [5].

(b) Ring array system by Waag and Fedewa [28].

Figure 2-1: Ring array systems

Ring transducers provide great image quality within the horizontal (in-plane) circular aperture (Fig. 1-1a), but the slice thickness (out-of-plane) is limited ($12mm$ in the CURE system) [5]. The difference in in-plane and out-of-plane resolution creates an anisotropic voxel sizes in the volumetric reconstructions, limiting imaging

to coronal breast slices.

2.1.2 Conical Arrays

To correct the anisotropic resolution in ring transducer systems and enable non-sliced 3D tomography, a conical array system for breast imaging was developed by Hopp et al. The conical system consist of 628 transmitters and 1413 receivers forming a $26\,cm$ diameter $18\,cm$ height semi-ellipsoidal aperture around the breast. Producing up to 80GB of data per scan on an FPGA-based sampling system, reflection, attenuation, and sound speed mapping is possible in spherical 3D coordinates [11]. The conical array is shown in Fig. 2-2.

Figure 2-2: Conical transducer array

With out of plane receivers, the conical array system can produce isotropic voxels in volumetric imaging. This enables extraction of transverse and sagittal volume slices shown in Fig. 1-1b, which is not possible in sliced based systems.

Relative to ring transducers, conical arrays have more transducer elements. DAQ and processing systems for the conical array is as complex, if not more complex, than the systems for ring transducers, but recent implementation of FPGAs and GPU processing has helped improve data throughput and processing [2]. The manufacturing complexity and cost of a conical array does not enable geometric flexibility in the system. Despite the transducer density, both the ring and conical arrays are still undersampling the slice or volume, respectively [23].

2.1.3 Array Probe Scanner

Mechanical sweeping with an array probe provides added system flexibility at the cost of scanning speed. Mechanical scanning with commercial array probes has been used for boundary detection for improving prosthetic fittings [4]. Commercially available probes do not support tomographic scanning and require an additional receiver to sample transmission data. Hansen et al. bypassed this limitation by adding an acoustic mirror opposing the transmitter [8]. Shown in Fig. 2-3, the stainless steel acoustic mirror reflects the incident wave back to the transmitter, providing through transmission data without a receiver. Ray tracing based on the arrival time of the reflected wave enables sound speed and attenuation mapping within the image slice.

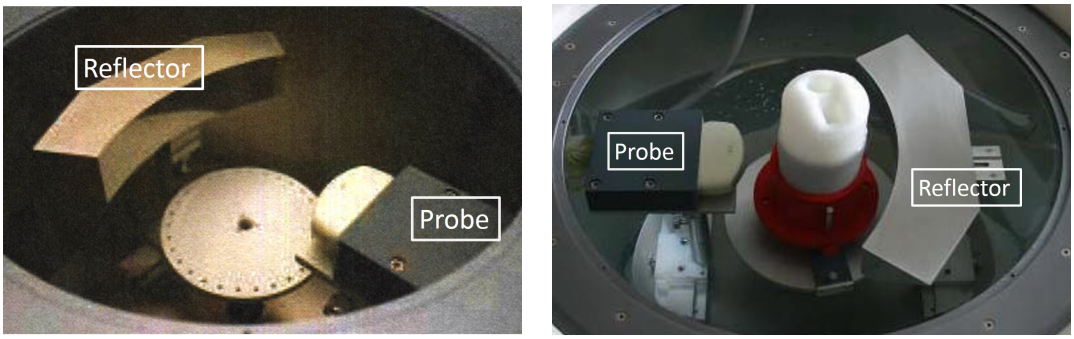

(a) (b)

Figure 2-3: Array probe with reflector [8]

Images (Fig. 2-4) are produced on the reflector system with as few as 3 insonifying angles (60°, 140°, 260°). Higher quality images are produced with 36 insonifying angles at 10° increments at multiple heights (Fig. 2-5) [10]

The reflector tomography system suffers from the slice thickness limitation as with the ring transducer system. The inability to capture off angle reflections limits imaging to coronal breast slices. From the cost perspective, commercial ultrasound probe and system costs ∼$10,000 per probe and ∼$100,000 to ∼$250,000 per system. Though likely cheaper than the ring array and conical array systems (pricing unavailable) $10,000 to exchange a transducer for testing and development is still non-trivial.

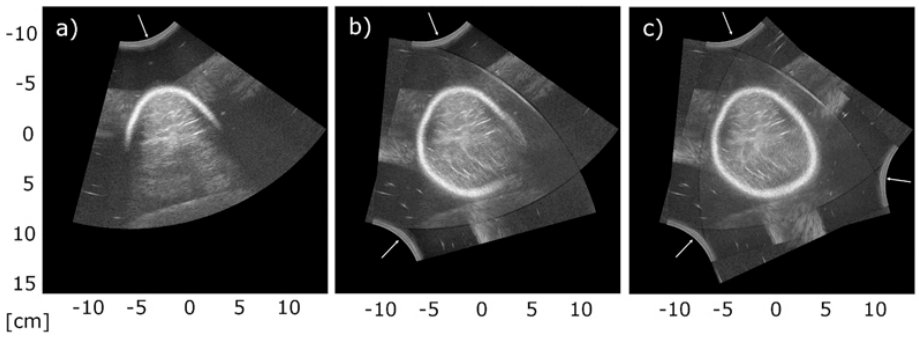

Figure 2-4: Reflector tomography

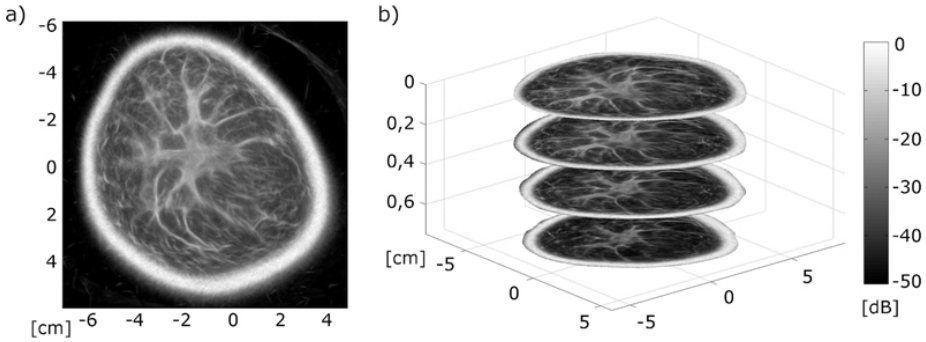

Figure 2-5: 36 angle reflector tomography at multiple heights

2.2 Single Element Scanning

For rapid iterative algorithm development, a system is required that is flexible and simple. The system should provide flexible transducer configurations (frequency/beam geometry) in conjunction with accurate transducer positioning. With high production cost and system complexity, ring and conical arrays are unsuitable for flexible iterative development. Array probes do provide more flexibility but cost is still high per probe (∼$10,000) and data acquisition flexibility is dependent on the corresponding probe imager manufacturer.

Single element scanning with one transmit and one receive channel is well suited at the developmental stages. Exchangeable transducers and single channel data acquisition significantly reduces cost and system complexity, while maintaining flexibility and low-level control of the system.

However, the flexibility and simplicity of a single element scanning system sacrifices the scanning speed. The transmit and receive transducers must be mechanically

placed at each sampling locations around the aperture to complete a scan. Mechanical positioning will always be slower than electronic switching but does allow for custom sampling resolution around the aperture. In reference to prosthetic fitting, as dicussed by Mak et al. [16], patient movement during a scan heavily affects the resulting image. Motion compensation or tracking may be necessary at lower scanning speeds to correct for patient motion.

2.3 Summary

An overview of ultrasound tomography was first given. Relevant tomographic systems using ring arrays, conical arrays, array probes, and single elements were discussed. Capabilities and limitations of each transducer architecture were presented and evaluated with reference to designing a developmental system for bone imaging. In conclusion, single element scanning offered the best flexibility, cost effectiveness, and simplicity for a developmental system. A summarized Pugh chart comparison with the ring transducer system as a reference is presented. in Table [TABLE]. Design, construction, characterization, and imaging with the selected system is presented in the following chapters.

Parameter	Ring	Spherical	Probe	Single
Flexibility	0	-	+	++
Simplicity	0	-	+	+
Cost	0	-	+	++
Speed	0	++	-	−
Sum	0	-1	2	3

Table 2.1: Comparison of system architectures

Chapter 3

System Requirements

In this chapter, the basic layout of a single element scanning system is first presented along with relevant transducer parameters. Based on the layout and the clinical motivations (Chapter 1), the purpose and requirements of the system are specified to constrain a deterministic design space. The functional requirements of the system are then defined and justified. Accordingly, concepts are developed and evaluated against the functional requirements.

3.1 Single Element Scanning Layout

A cylindrical aperture is preferred over a semi-spherical aperture to reduce the complexity of the mechanical positioning system. With two single element transducers, a cylindrical aperture can be created with a combination of rotatory and linear positioning systems (rotary tables, linear sliders, lead screw drives, etc); whereas, creating a spherical aperture requires more complex mechanical designs (robotic arms) to define the motion axises. For imaging, the spherical system [11] overcomes the slice thickness limitations of the ring transducer system [5] by capturing out-of-plane transmissions with additional receivers. However, if the single element transducers are able to move relatively out-of-plane in a cylindrical aperture, the out-of-plane transmissions could be captured as well. The layout of a single element system in cylindrical coordinates is presented Fig. 3-1.

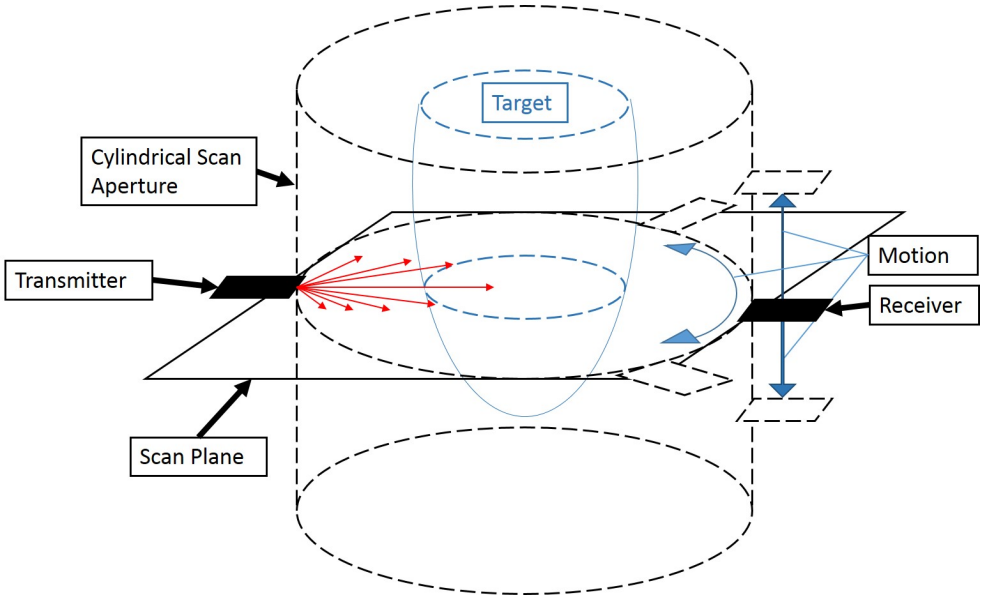

Figure 3-1: Cylindrical Scanning Layout

3.2 Transducers

The image quality of an acoustic scanning system is heavily dependent on the transducer parameters. Particularly, the frequency and beam geometry will directly affect the depth of penetration and the image resolution, respectively. An example beam geometry of a focused single element transducer is presented in Fig. 3-2 for clarification.

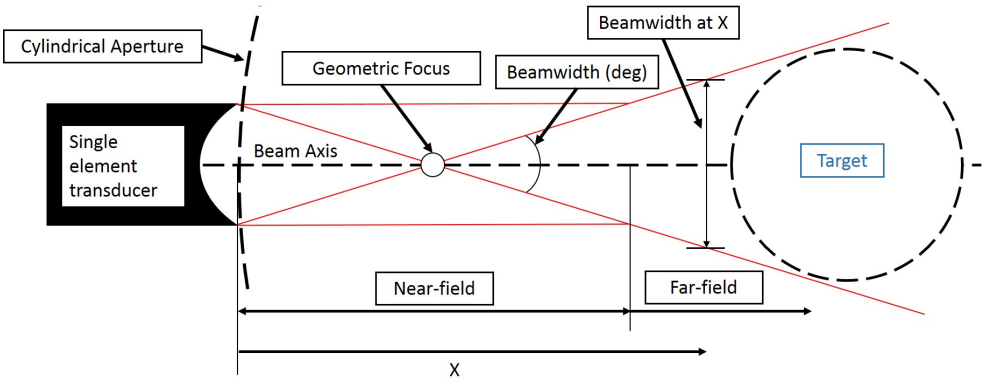

Figure 3-2: Cylindrical Scanning Layout

3.2.1 Focus

The geometric focus point is defined by the physical curvature of the transducer lens and governs the length of the near-field, beamwidth, and beam spread [26]. The near to far-field transition locates the maxima of the transmitted acoustic wave and begins beam spreading and the decrease in wave amplitude [26]. The transducer focus should be carefully selected to ensure ample coverage of the target in the cylindrical aperture.

3.2.2 Frequency

Independent of the focus, the transducer frequency (f) directly contributes to the image resolution. The wavelength (λ) of the transmitted wave is inversely proportional to the transducer frequency by λ=c/f, where c is the speed of sound in the medium. With idealized single pulse transmissions, the best spatial resolution on the beam axis (axial resolution) is defined as $\lambda/2$ [26]. For example, a $5MHz$ transducer scanning in water (c∼$1500m/s$) would have a wavelength of λ=$300\mu m$ and an axial resolution of $150\mu m$. The resolution perpendicular to the beam axis (lateral resolution) is defined by the beamwidth, dependent on beam spread and the object distance from the transducer.

Frequency also affects penetration depth into the target. Attenuation of ultrasound during propagation through a medium is frequency and distance dependent. Typical acoustic attenuation coefficients in biological tissue is shown in Table. 3.1.

Tissue	Attenuation coefficient ($dB/MHz/cm$)
Cancellous bone	10 - 40
Cortical bone	1 - 10
Fat	0.8
Muscle	0.5 - 1.5
Skin	2 - 4

Table 3.1: Attenuation coefficient of various biological tissues [14]

In comparison, bone is significantly more attenuating than soft tissue. Diagnostic ultrasound devices in soft tissue range from 2 to $15MHz$ in frequency, whereas clinical

bone devices range from 0.25 to 1.25MHz [14]. For the clinical motivations discussed in Chapter 1, the transducer frequency should accommodate transmission through bone without sacrificing too much spatial resolution in the muscle layers. The highest transducer frequency expected would be at 5MHz. For transmission through a 3cm thick cortical bone with average attenuation of 5$dB/MHz/cm$, a 5MHz signal would be attenuated by 75dB. This attenuation is high but still recoverable with current signal amplifiers. Cancellous bone may further limit the frequency but the attenuation is highly variable due to variability in the bone porosity [7]. Multiple frequency transducers may be necessary to separately accommodate each motivating clinical need.

3.3 Functional Requirements

Design Purpose: To develop a flexible tomographic acoustic imaging system that supports rapid algorithm development.

3.3.1 Primary Functional Requirements

To achieve the desired system characteristics, the following functional requirements are imposed on the system. Developed concepts should minimally satisfy the primary functional requirements to be considered.

1. *Scan Aperture/Angular DOF.* In sliced tomographic scanning, the transmit and receive positions must independently enclose the scan target. Corresponding to this, the system transducer transmitter and receiver positioning must form an cylindrical aperture around the scan target.

2. *Axial DOF.* To enable 3D volume scanning, the transducers must move axially along the length of the target.

3. *Independent Motion.* Transmitter and receiver positions must be independently reconfigurable to form any desired transmit receive pairing in the scan volume.

In conjunction with the angular and axial DOF requirements, the system must control four DOFs, two for each transducer. One transducer must not interfere with the other.

4. *Accurate Positioning.* Since image quality is directly related to transducer positioning, the system must accurately position the transducers during scanning. For the target applications, the highest frequency expected is $5\,MHz$, corresponding to an axial resolution of $150\mu m$. Therefore, the transducer positioning error must be below $150\mu m$.

5. *In-vivo Subject Scanning.* System layout must allow scanning of *in-vivo* targets.

6. *Flexible.* Transducers should be easily exchangeable to enable testing of varying transducer frequencies and beam geometries.

7. *Safe.* The system must be safe for human subjects. Moving mechanical components should not be in close proximity of the patient body and acoustic power of the transducers must be within FDA limits.

3.3.2 Secondary Functional Requirements

Beyond the primary functional requirements, secondary functional requirements were outlined for further evaluation of developed concepts.

1. *Cost.* The total system cost should be minimized. Where MRI systems could cost up to five to ten million dollars, typical ultrasound systems are ∼$150K. For a developmental system, we decided to limit our total cost to ∼$30K.

2. *Simplicity.* The system should not be unnecessarily complex. Concept were evaluated in simplicity based upon the number of components, the number of custom parts, and the assembly procedure.

3. *Speed.* Scanning speed is important to produce images on a clinically relevant time scale. However, for a developmental system, image quality should be proven before scanning speed emphasized.

3.4 Concepts

With the primary and secondary functional requirements in mind, the following concepts were developed.

3.4.1 Concept A

As seen in Fig. 3-3, two large ring bearings are used to define the rotational motion while two brackets with linear sliders are used to define the axial motion. Since two independent rotations are required (transmitter and receiver), two ring bearings are necessary. For axial motion, transducer brackets with sliders and lead screws can be used to move each transducer.

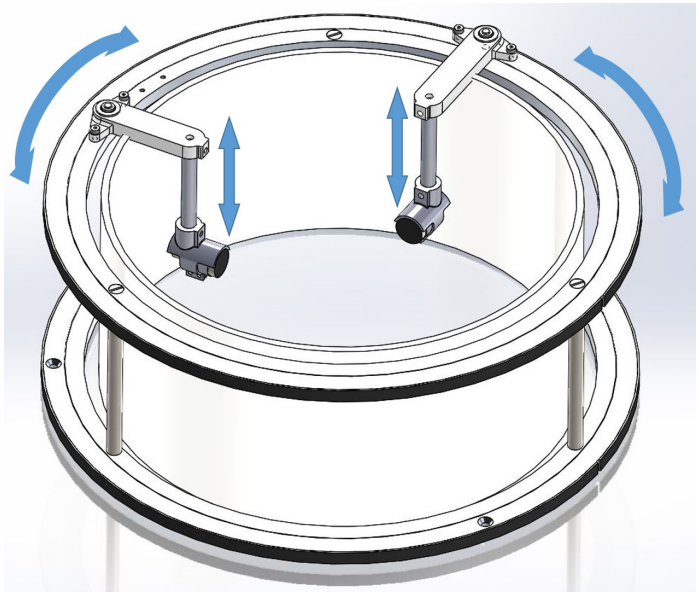

Figure 3-3: Dual ring bearing

3.4.2 Concept B

Instead of using two separate bearings to define two independent rotations on the same path, Concept B uses a single track to define the path while independent carts move on the path. As shown in Fig. 3-4, the geared dual v-groove track (yellow) defines the path while two carts independently move on the track. Similar brackets

shown in Concept A can be used for axial motion.

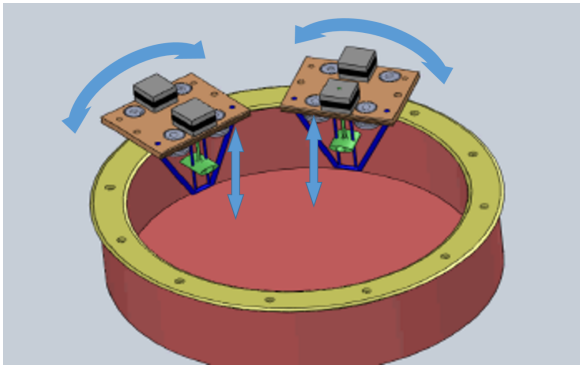

Figure 3-4: Tracked design

3.4.3 Concept C

Instead of ring bearings, Concept C uses two small bearings below the water tank. Extension arms holding each transducer reach from the bearings into the tank. Again linear sliders can be used for vertical motion on the arms.

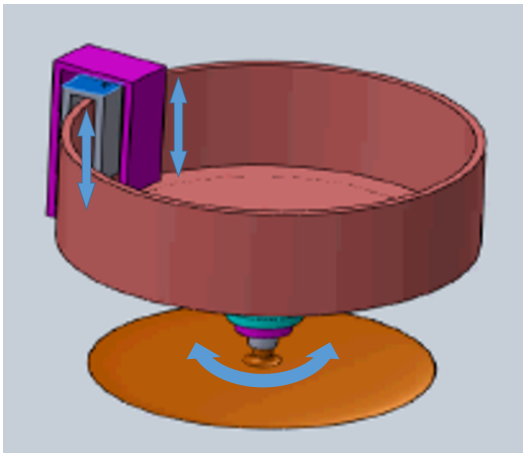

Figure 3-5: Dual arm design

3.4.4 Concept D

Building upon Concept C, the length of the arms can be reduced by protruding the arms through the tank base with water sealed bearings.

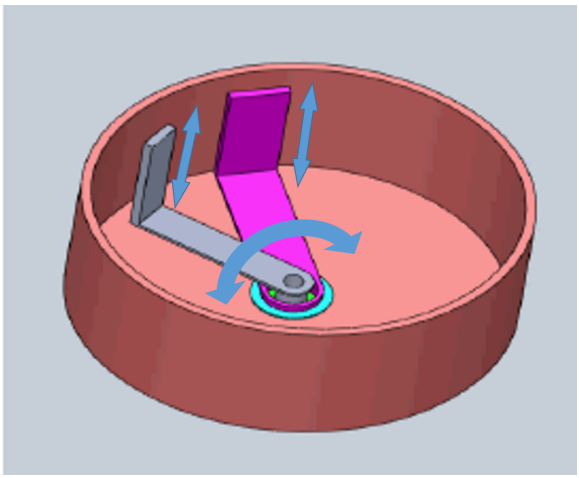

Figure 3-6: Through tank design

3.4.5 Concept E

Instead of moving the transducers, the entirety of the tank can be moved with the traducers attached on linear sliders.

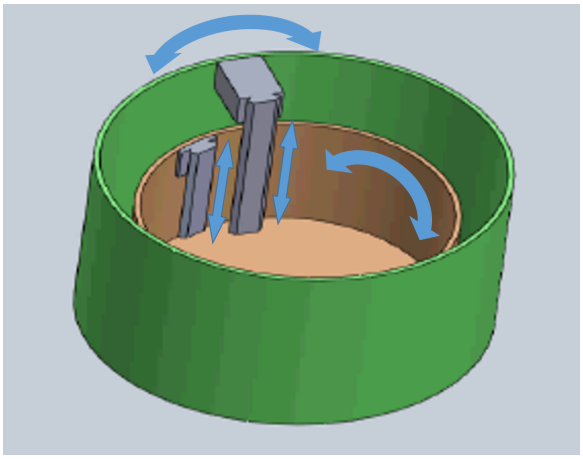

Figure 3-7: Nested tank design

3.5 Concept Selection

Concepts were evaluated against the primary and secondary functional requirements in a weighted Pugh Matrix. Primary functional requirements were weighted more heavily to emphasize satisfaction of the overarching design purpose. Concept A was

selected as the baseline for comparison. All motion related functional requirements were grouped into "Motion" to improve clarity.

3.5.1 Summarized Pugh Chart

FRs	Weight	Base (A)	(B)	(C)	(D)	(E)
Motion	2	0	0	0	0	0
Accuracy	2	0	1	-2	-1	-1
In-vivo scanning	2	0	0	0	0	0
Flexible	2	0	0	0	0	0
Safe	2	0	0	-1	-2	-1
Cost	1	0	-2	-1	-2	-2
Simplicity	1	0	-1	-2	-2	-2
Speed	1	0	0	0	0	-2
	Sum	0	-1	-9	-10	-10

Table 3.2: Concept Selection Pugh Chart

In comparison, all concepts satisfy the primary functional requirements, with variations in accuracy and safety. Concept C and D were rated lower in accuracy since the structural path from the bearing to the transducer is longer relative to Concept A. Concept E is lower in accuracy since the inertia of the entire water tank must be moved to move the transducer; deflections are expected to be higher from heavier loading on the motion components. Concept D had the lowest rated safety due to the transducer arms at the tank bottom forming a pinch point near the scan target. Concept C and E were also lower in safety due to supporting the water tank on a smaller base and requiring to move a large mass, respectively. First order designs and reasonable cost estimates were used to compare the secondary requirements. Generally, Concept C, D, and E were worse in cost and simplicity due to the number of custom components required. Speed was generally the same for all except concept E which moves a significantly higher mass.

In summary, Concept A was the best rated and Concept B was a close second. Concept B shows classical trade-off between accuracy, cost and simplicity. However, at this design size, machining of high precision components significantly increases the

overall cost. In conclusion, Concept A was selected for more further development. Concept B could be explored in the future to improve accuracy.

3.6 Summary

The functional requirements for a 3D single element tomographic system were outlined and the corresponding constraints were defined to guide the design process. Primary and secondary functional requirements were separated to better evaluate concepts. Five design concepts enabling independent transducer positioning were developed and modeled in CAD. Evaluation of the concepts against each other and the functional requirements was completed via a weighted Pugh matrix. Concept A (dual ring bearing) was selected for further development.

Chapter 4

Detailed System Design

In this chapter, we present the detailed mechanical and electrical design of the system. The necessary transducer DOFs are defined and the corresponding motion control strategy is presented. Design for each component is first presented in Solidworks, followed by the final physical prototype. Major design decisions are evaluated following the primary and secondary functional requirements and the defined design purpose. Electrical design in this chapter focuses on the motion control system; electrical design of ultrasonic data acquisition for imaging is discussed in Chapter 5.

4.1 Scanning Tank

For volumetric limb imaging, a scanning tank must hold the patient limb, two transducers, and the coupling medium. A medium is necessary acoustically couple transducer to the patient limb. Ultrasound gel is used for contact probe, but for this large scale, a water tank can be used to immerse the limb and transducers. Deionized water is preferred for accurate calibrations and reducing variations in the speed of sound [1]. A $16in$ diameter and $7.5in$ long clear acrylic tube was glued (Weld-On 4) to an $0.5in$ acrylic plate to create the scanning tank. The cylindrical section holds the deionized water while the acrylic base serves as the system base to attach the motion structures.

4.2 Transducer Degrees of Freedoms (DOF)

In volumetric imaging, transducer DOFs are dictated by the scan aperture. In the cylindrical aperture defined in 4-1, independent angular and axial transducer DOFs are necessary. Similar to the ring transducer setup [5], arbitrary transmit and receive pairs must be possible within a single horizontal scan plane. In addition, as discussed by Hopp et al., out of plane transmit and receive pairs are necessary for reducing slice thicknesses [11]. In total, four DOFs are necessary in the system, an angular and an axial DOF for each transducer.

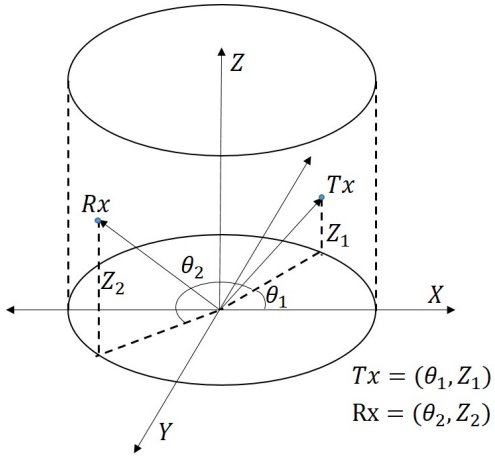

Figure 4-1: Scanner 3D coordinate system.

Note: Receiver position is relative to the transmitter position instead of the zero reference.

4.3 Angular Motion

To sweep circumferentially around the target, two bearings can be used to define the circular trajectory. To accommodate a patient limb transducer bracketing, and wiring, the the bearings should be around $500mm$ in diameter. Two options are available: geared slewing bearings and ring bearings. Slewing bearings at this scale are designed for heavy-duty applications such as: industrial machinery, aerospace and defense, and medical systems (MRI, CT). To move these heavy loads, slewing bearings are stiff and

are typically geared internally or externally for actuation. Slewing bearings provide great stiffness and accuracy but are heavy ($\sim 100 lbs$) and costly ($\sim$\$4000) at the $500mm$ scale (www.kaydonbearings.com). For our application, loads induced from moving transducers are relatively small and do not require the high load ratings. Thin ring bearings (Lazy Susan's) are more fitting for these smaller loads. Light and low-cost, ring bearings have both the necessary trajectory and support sufficient loads. However, these ring bearings are not geared nor typically evaluated for error motions. Additional testing and validation (Chapter 6) will be necessary to ensure positioning accuracy within the defined $150\mu m$.

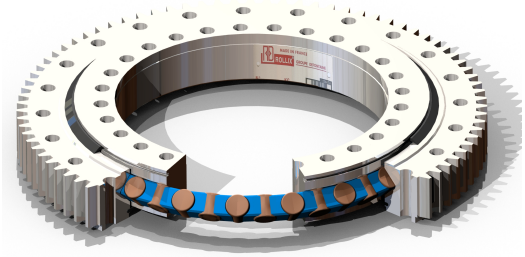

(a) External geared slewing bearing

(b) Lazy Susan bearing

Figure 4-2: Bearings choices for angular rotation

4.3.1 Bearing Layout

For the two transducers in the system, two ring bearings are necessary for independent angular movements. As defined in Fig. 4-1, the transmitter position (θ_1) is relative to the system ground, whereas the receiver angular positioning (θ_2) is relative to the transmitter. Therefore, the transmitter bearing must be reference the system ground while the receiver bearing must reference transmitter bearing. Shown in 4-3, the outer race of the bottom bearing is rigidly connected to the tank base (ground) while the inner races are rigidly connected to each other. In this bearing layout, the inner race of the top bearing defines angular position of the transmitter while the outer race of the top bearing defines the angular position of the receiver. This couples the two angular motions. This is acceptable since knowing receiver positioning relative to the transmitter is more important than knowing the absolute positioning of both transducers.

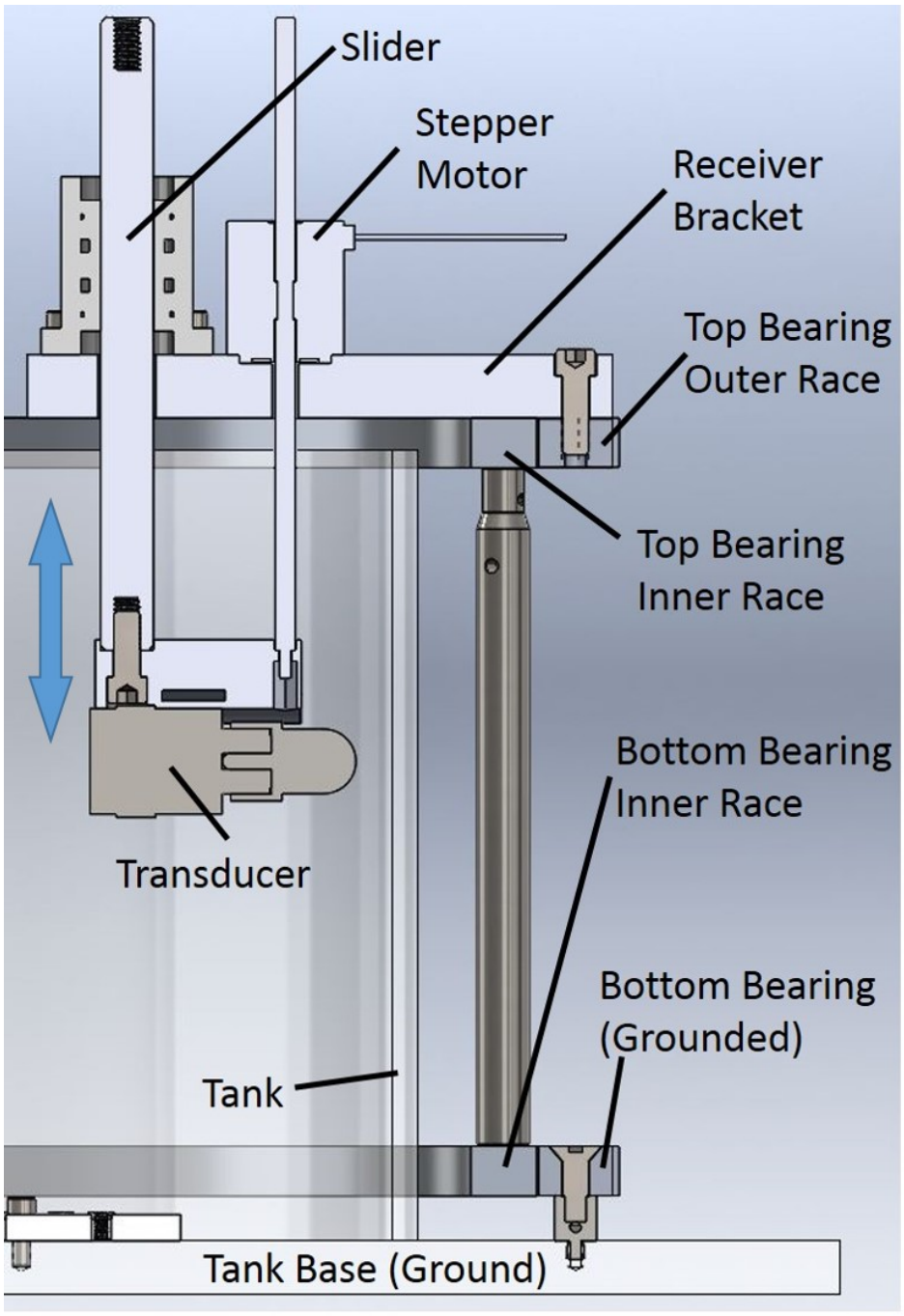

Figure 4-3: Cross section of transducer bracket

4.3.2 Angular Motion Control

For angular motion control, actuation of and feedback from the ring bearing is needed. Since the ring bearings are not geared, a friction pinion drive system is necessary for actuation. For the best accuracy, direct feedback on the ring bearing was chosen over indirect feedback on the drive pinion. As seen in Fig. 4-4, the friction pinion, driven by a brushless DC motor (Maxon), actuates the outer races and a high resolution ($\sim 1\mu m$) magnetic encoding setup (Renishaw: LM10 encoder, LM10ECL00 encoding tape) provides the feedback. Actuation and encoding for the top and bottom bearings are identical, with the exception the bottom bearing actuation is inverted to reduce space.

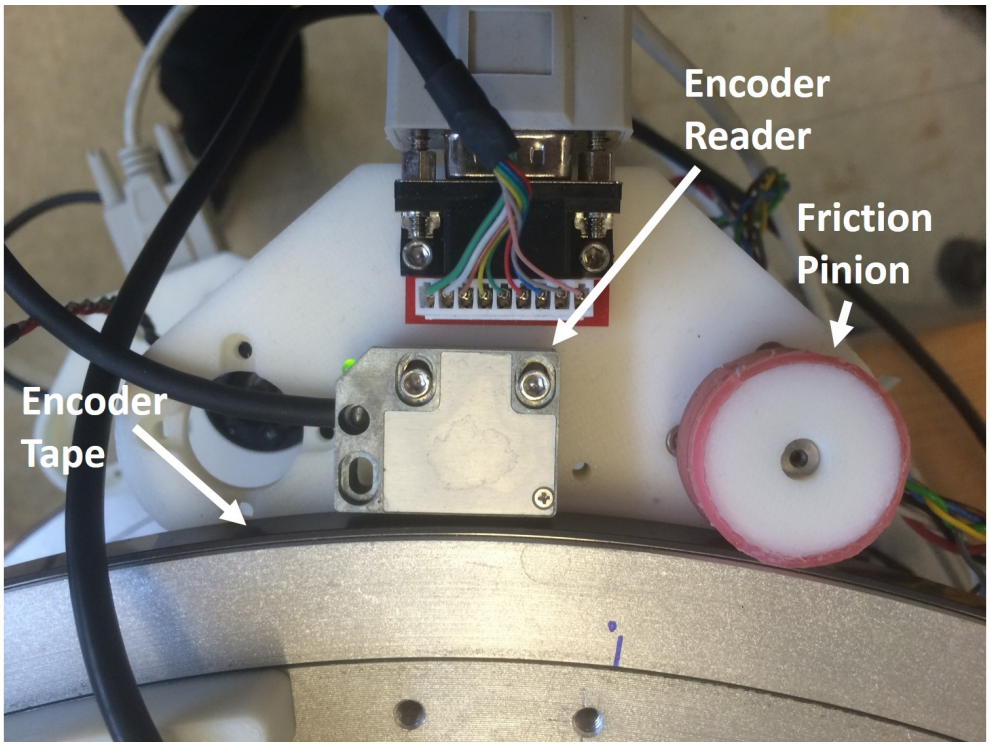

Figure 4-4: High resolution encoding setup and drive pinion

Closed-loop position control is implemented by an NI myRIO microcontroller in LabView. The myRIO features a customizable Xilinx FPGA in addition to the main dual-core processor. The FPGA converts the quadrature signal from the LM10 encoder to counts and the processor samples the count on each loop-iteration. For actuation of the brushless motors, two Maxon motor drivers (Maxon PART NUM-

BER) with internal speed controllers were added. A simple proportional derivative (PD) controller implements closed-loop position control. The myRIO reads the current position on the FPGA, compares it to the desired reference, and outputs the desired motor speed to the driver. The gains are tuned to minimize overshoot to eliminate extra triggering (discussed in Chapter 5). Since the encoder tape is not absolute, a reference was marked on the bearing to zero the system during initialization. Since the system is cylindrically symmetric, an arbitrary zero position can be selected. LabView VI for a single motor controller is shown in Fig. 4-5.

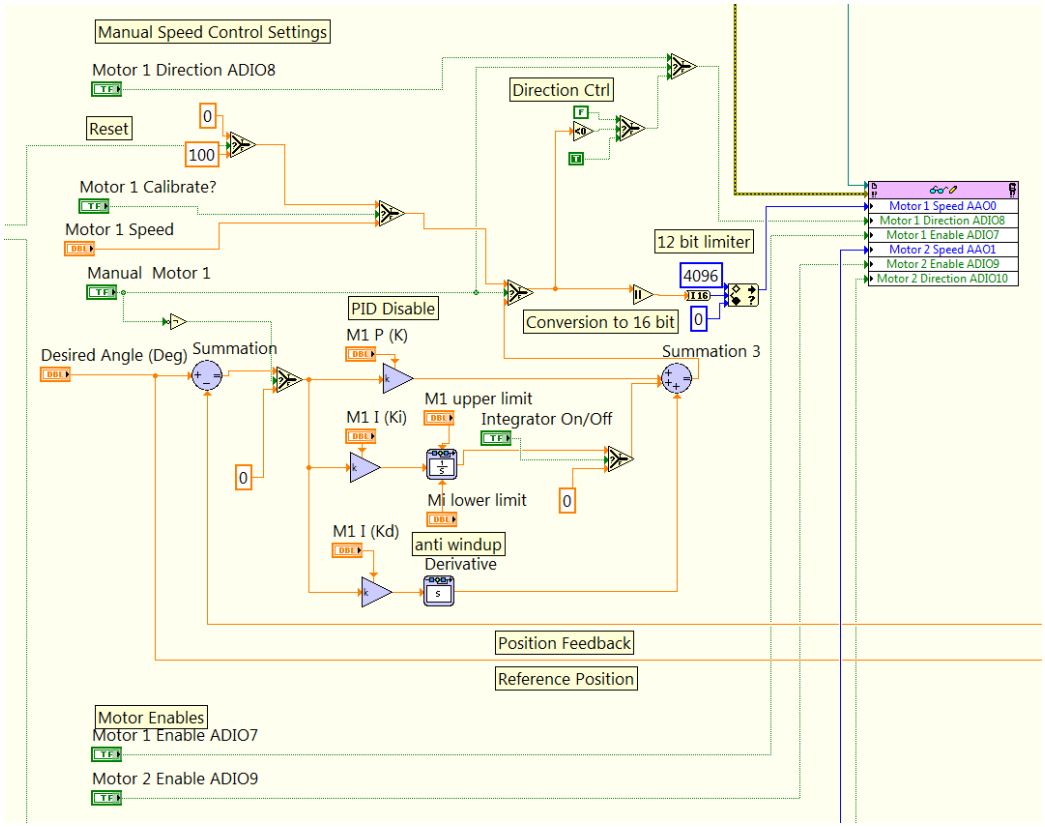

Figure 4-5: LabView angular control VI for a single motor

4.4 Axial Motion

To move transducers axially along the tank depth, two transducer brackets were designed. The bracketing should constrain five DOFs and only allow axial translation of the transducers. As seen in Fig. 4-3, the fixed-alignment linear bearing and slider shaft constrains the transducer holder in four DOFs, allowing free translation along the shaft and rotation about the shaft. To constrain rotation and add actuation, a non-captive stepper motor (HaydonKerk) was added. The non-captive motor allows movement of the threaded rod relative to the fixed motor during actuation. The non-captive stepper motor (HaydonKerk) has sufficient shaft play to self-align to the linear slider; this constrains the rotational DOF without over-constraining the holder. However, some rotational play still exists but is negligible for the small drag forces during movement through the water. Transducer bracketing is identical for both transmitter and the receiver, with the exception the receiver fixturing is shortened to adjust for placement on the top bearing inner race instead of the outer race. Holders on both brackets use band clamps to fixture the transducers. Transducers can be easily exchange and custom shapes can be 3D printed to accommodate a wide variety of transducer form factors.

4.4.1 Axial Motion Control

Since no feedback is available for the non-captive stepper motors, axial positioning is done in open-loop on the myRIO running LabView. Similar to angular motion control, an arbitrary axial position can be selected as the zero position during initialization. Dedicated stepper drivers (Pololu A4983) provide power and converts the input rising edges to steps on the motor. As shown in Fig. 4-6, the myRIO VI reads the desired number of steps from the user, then sends square wave pulses until the corresponding number of rising edges have been sent. With on/off currents in the stepper motor coils during movement, the energized coils radiate electromagnetic waves. Sufficient shielding must be present in the transducer cabling to reduce electromagnetic noise in the signal.

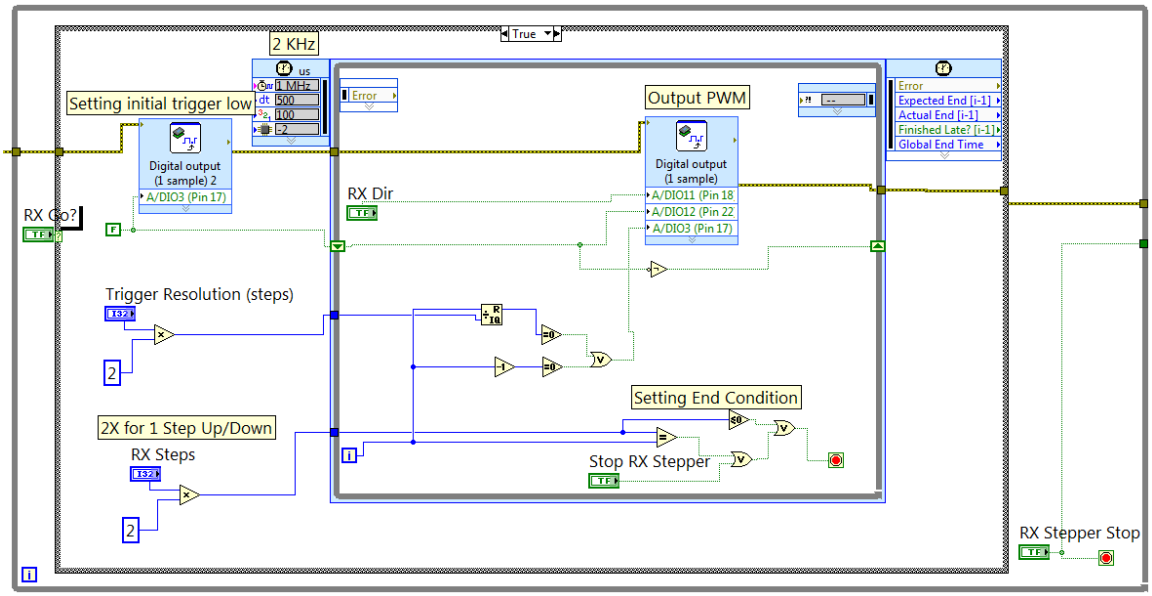

Figure 4-6: LabView stepper control VI

4.5 Summary

The fully assembled system, including the DAQ hardware is shown in Fig. 4-7.

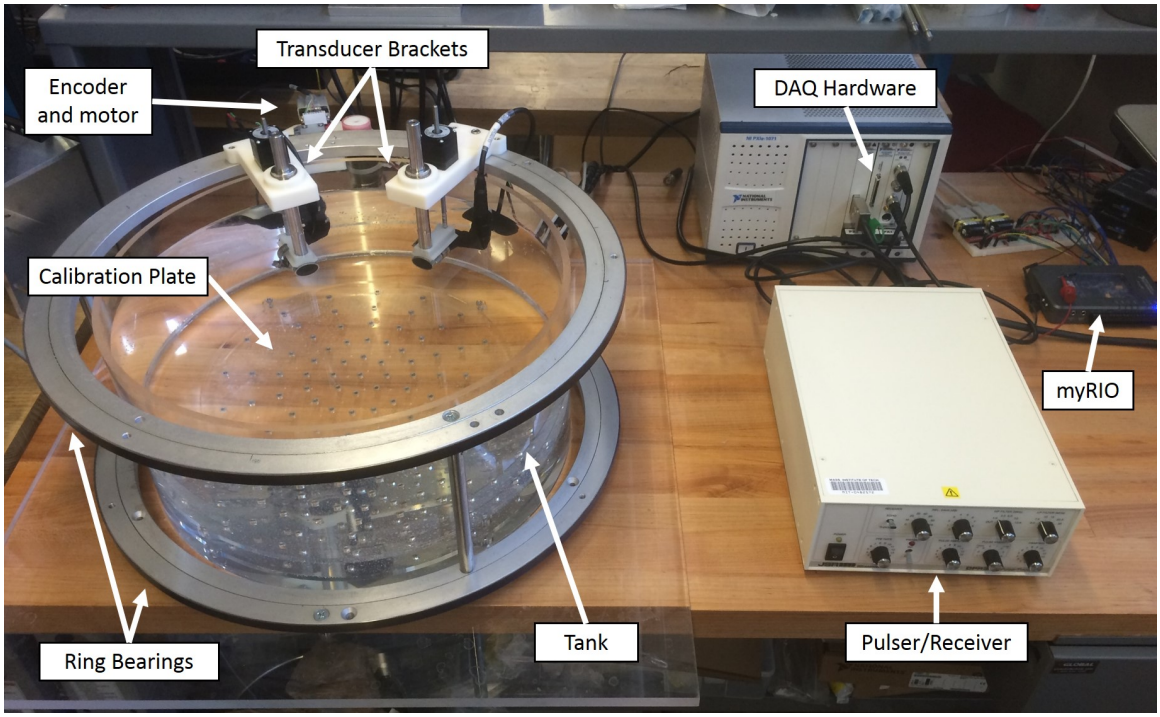

Figure 4-7: Full scanning system with calibration plate

Chapter 5

Data Acquisition Design

One of the biggest challenges in ultrasound tomography is the sheer amount of data collected in the system. For a sufficiently sampling ring or spherical breast ultrasound system, data quantities can reach up to $103\,GB$ or $97\,TB$ of data per scan, respectively [23]. Multi-transducer systems in [5] and [11] must sample all receive channels in parallel. The designed single element system only needs to sample data through one receive channel. This significantly reduces DAQ hardware cost and reduces system complexity. However, single channel streaming does not reduce the total amount of data per scan. In addition, single channel acquisition increases the total scanning time by requiring mechanical positioning of the single transducer at all receive locations and transmit locations. Nevertheless, for a cost effective algorithm development focused system, flexibility in transmitter and receiver pairing is more important than scanning speed. Scan time reduction by novel sampling strategies [25] will be explored in the future but is outside the scope of this thesis. In this chapter, we present the system data acquisition design for the single element system including: transducer selection, pulse emission, system synchronization, data sampling, and data streaming.

5.1 Transducer Selection

For calibration and initial imaging, two identical single element transducers were selected for transmission and receiving. As discussed in Chapter 3, wavelength is

inversely proportional to the frequency and defines the spatial resolution, higher frequency transducers are necessary to have sufficient spatial resolution to calibrate system positioning errors. We selected a 60% bandwidth (at -6dB) 5MHz transducer for initial scanning and calibration. This frequency and bandwidth gives the best spatial resolution while maintaining emission of lower frequency bands for transmission through bone.

To enable testing of tomographic methods such as ray-tracing or attenuation mapping, wide beamwidth or omni-directional transducers are needed. For these methods, the transmitted beam front should cover the smallest boundary circle (BC) enclosing the target cross section at the center of the tank. With the frequency and beamwidth specification, we selected the Olympus V308-SU transducer with focus at 1in for initial testing (Figure 5-1b). Transducers are easily exchangeable on the holder; various frequencies and beam geometries can be tested in the future.

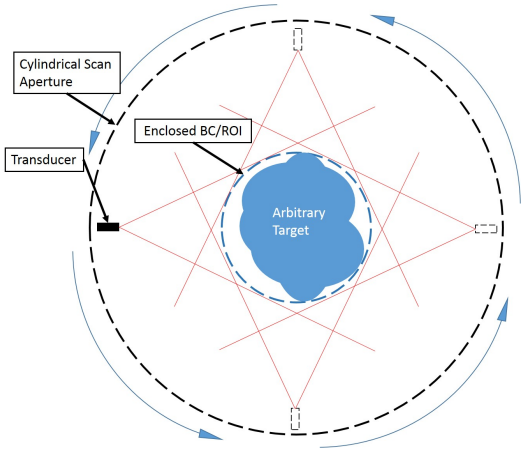

(a) BC enclosed by a wide beamwidth transducer

(b) Focused single element 5MHz transducer

Figure 5-1: Focused 5MHz transducer and the enclosed BC

5.2 Pulser/Receiver

For ultrasound transmission and reception, a low frequency pulser/receiver (JSR Ultrasounics DPR300) was selected. The DPR300 shock excitation pulser/receiver is switchable between pulse-echo and pitch catch modes, and has flexibility in the trans-

mit pulse duration, pulse amplitude, damping, and control over the receive amplification and filtering.

5.3 High Speed Data Acquisition

As previously discussed, total data quantities can reach many gigabytes. Typical scopes have do not hold sufficient on-board memory to accommodate such large data quantities. High speed transfer from the scope to a host PC is necessary to prevent data loss.

5.3.1 Data Rate

A first-order estimate of data rates in a single slice pulse-echo scan was used to estimate necessary data transfer rates. For a $5MHz$ transducer sampled $50MHz$ with 14-bit resolution, a single pulse-echo amplitude modulation scan (A-scan) of a $500mm$ diameter tank would produce $43.7kB$ of data. Scanning the $500mm$ diameter circular aperture with $\lambda/2$ ($150\mu m$) sampling resolution produces 10467 A-scans. Reasonably limiting a single slice pulse-echo sequence to 5 seconds, each sweep generates about $90MB/s$. This data rate is significantly higher than the maximum transfer speeds of USB 2.0 DAQs interfaces ($60MB/s$). PCI Express bus ($500MB/s$) based DAQs are necessary to accommodate these high data rates. (*Note: USB 3.0 DAQs are sufficient and available but were not selected due to similar pricing for slower data transfer speed when compared to PCI Express*)

5.3.2 Digitizer

For ease of system integration in LabView, a high speed NI digitizer card (PXIe-5122) was selected to sample data output from the DPR300 pulser/receiver. In addition, the designed NI PXI chassis incorporates a PCI Express link to the host PC (PXIe-8270), ensuring high data transfer speeds. The PXIe-5122 provides 14-bit sampling resolution up to $100MHz$ maximum.

5.4 Synchronization

For data acquisition timing, all components of the system must be synchronized to when the ultrasound transmitting transducer is triggered on the DPR300. In fixed height pulse-echo scanning with uniform sampling, the transducer must emit and receive pulses at fixed angular increments around the scan object. In pitch-catch mode, the transmitter must emit when the receiver has moved a fixed angular increment. Regardless of scanning mode (pulse-echo for backscatter scanning or pitch-catch for tomographic scanning), the system should be triggered based upon the location of the transducer with respect to the desired sampling resolution. Angularly, the trigger signal will be dependent on the encoder count. Axially, the trigger signal will be dependent on the step number. Both the encoder count and the step number is recorded within the myRIO. When the trigger condition of the count or step increment is met, the myRIO control virtual instrument (VI) will automatically send a square wave pulse to trigger both the DPR300 and the PXIe-5122.

On the myRIO, the desired step and count increments between each trigger are set before control is initiated. Axial triggering based on the step increment is done directly in the main control VI; however, angular triggering is done on the FPGA. Due to the high encoder resolution ($1\mu m$), the encoder count on the FPGA changes significantly faster ($40MHz$) than how fast the control VI can sample ($1kHz$). If the trigger condition is dependent on the count sampled by the control VI, many angular triggers would be missed. To eliminate the sampling discrepancy, the angular triggering is directly implemented in hardware on the FPGA. As shown in Fig. 5-2, the myRIO FPGA VI first converts the LM10 quadrature output to counts; if the count is matches the trigger condition, the square wave trigger pulse will sent. An additional line driver (Texas Instruments CD74AC244E) was added on the myRIO trigger output to supply sufficient power to drive the DPR300 and the PXIe-5122 trigger inputs. Full layout of the data acquisition schematic is shown in Fig. 5-3 (line driver not shown).

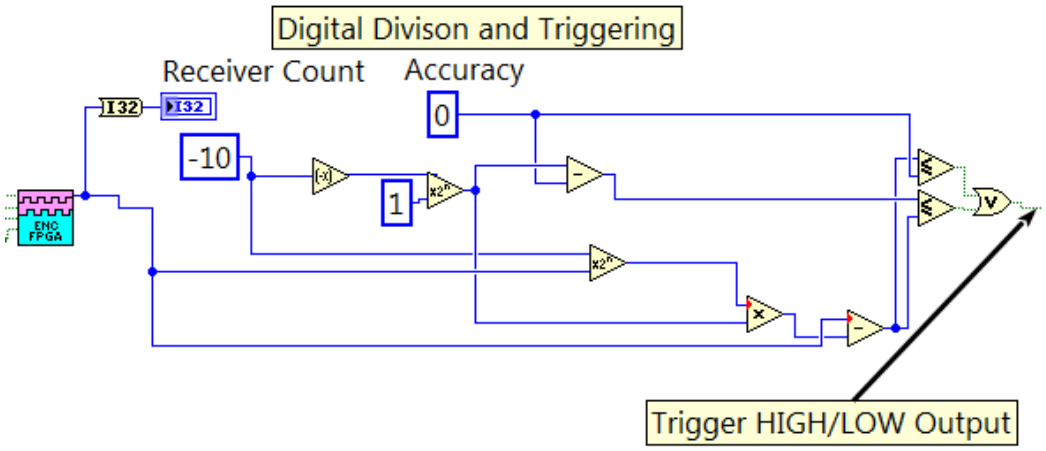

Figure 5-2: Custom FPGA personality for high speed triggering

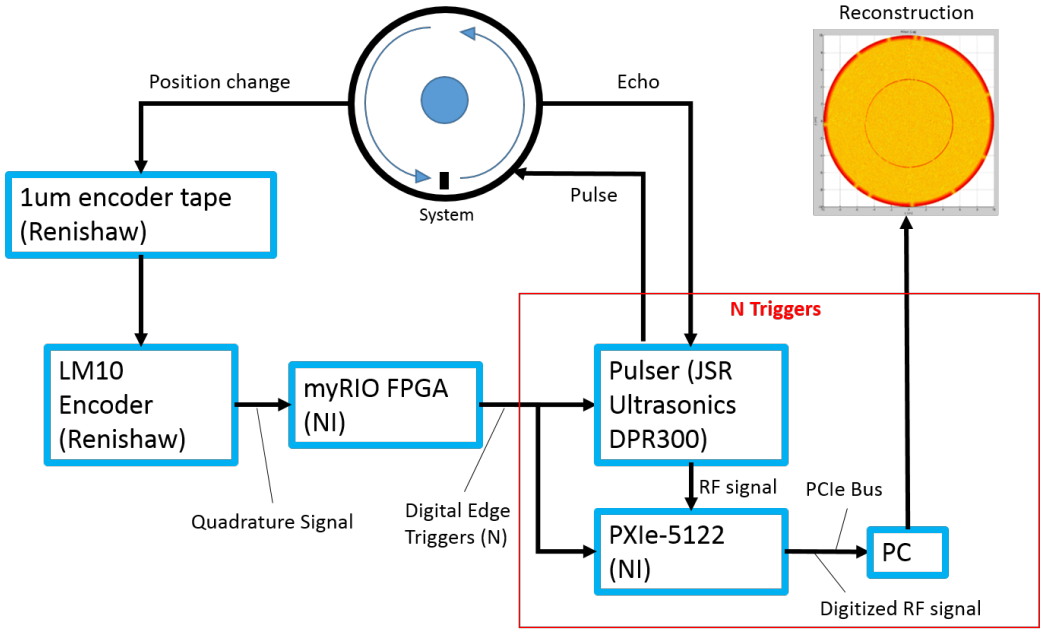

Figure 5-3: DAQ schematic and synchronization

5.5 Summary

A $5MHz$ transducer has been selected for initial testing of the system. To accommodate expected data rates and volume, a high speed DAQ hardware was designed, assembled, and synchronized to the encoder position count on the FPGA which is recording transmit location.

Chapter 6

System Characterization

Variations and error in the mechanical assembly, transducer characteristics, and data sampling all contribute to degradation and error in the final image quality of the system. Each of these error sources must be accounted for to evaluate and correct for aggregate errors in the system. In this chapter, we present a characterization of the error sources including transducer positioning errors, DAQ instabilities, and speed of sound (SoS) variations. In addition, the actual transducer beamwidth was simulated in a finite element (FE) software (PZflex) and measured to quantify the actual covered ROI.

6.1 Error Sources

To establish a ground truth, calibration fixtures of known geometry (cylindrical rods/threads) fastened at fixed locations on the threaded calibration plate (Fig. 6-1) were scanned (pulse-echo, $5MHz$ transducer).

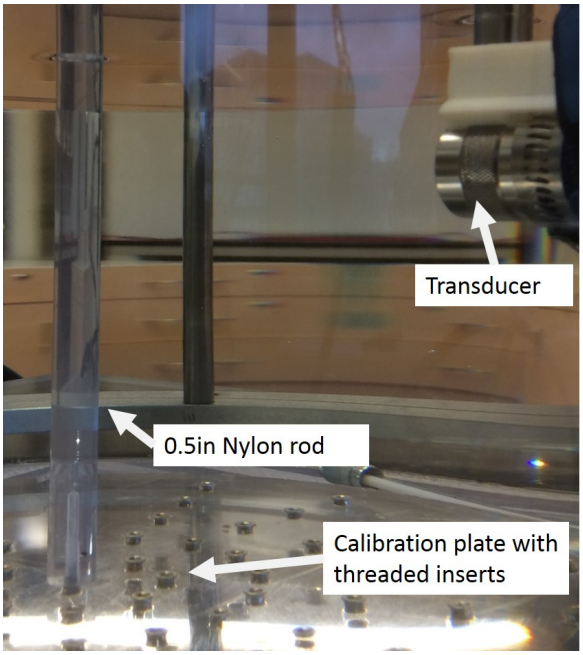

Figure 6-1: $0.5in$ nylon 6-6 rod centered in the tank on the calibration plate.

Using the coordinate system defined in Fig. 4-1, the position of a scatterer in pulse-echo scanning in a single horizontal plane is

$$s(\theta) = R(\theta) - C * t(\theta)/2 \tag{6.1}$$

For each angular position θ, s is the distance of a scatterer from the center of the tank, R is the radial position of the transducer, C is SoS, and t is the two-way travel time of the received echo. To separate error contributions from each input, partial derivatives of Eq. 6.1 with respect to each variable is analyzed to define an error budget for each respective input. Total alloted error is bounded by the minimum acoustic resolution of $150\mu m$ $(5MHz)$.

$$ds = \frac{\partial s}{\partial t}dt + \frac{\partial s}{\partial R}dR + \frac{\partial s}{\partial C}dC \leq 150\mu m \tag{6.2}$$

Following Eq.6.2, the total error is the summation of each partial derivative multiplied by the respective deviation. To satisfy the total $150\mu m$ alloted error, equal $50\mu m$ contribution is alloted for each input. Using expected mean values for each parameter, reasonable error bounds can be defined for each input. With expected SoS in water around $1500m/s$ [1] and maximum travel time around $200\mu s$ in the scanning aperture, the following bounds can be established.

Partial	Estimate	Bounds	Source
$\frac{\partial s}{\partial t}dt = \frac{C}{2}dt$	C$\approx$1500m/s	$dt \leq 67ns$	DAQ instability
$\frac{\partial s}{\partial R}dR = 1dR$	None	$dR \leq 50\mu m$	Position error
$\frac{\partial s}{\partial C}dC = \frac{t}{2}dC$	$t_{max}\approx 200\mu s$	$dC \leq 0.5m/s$	SoS variation

Table 6.1: Alloted error for each input

6.1.1 DAQ Stability

To characterize the DAQ sampling measurement stability, 2000 pulse echo A-scans were captured with the transducer and the target at a fixed separation. Temporal location of the first echo envelope peak was detected, shifts in the peak location within the 2000 A-scans were recorded to characterize DAQ stability. Measurements were repeated 9 times at varying separations.

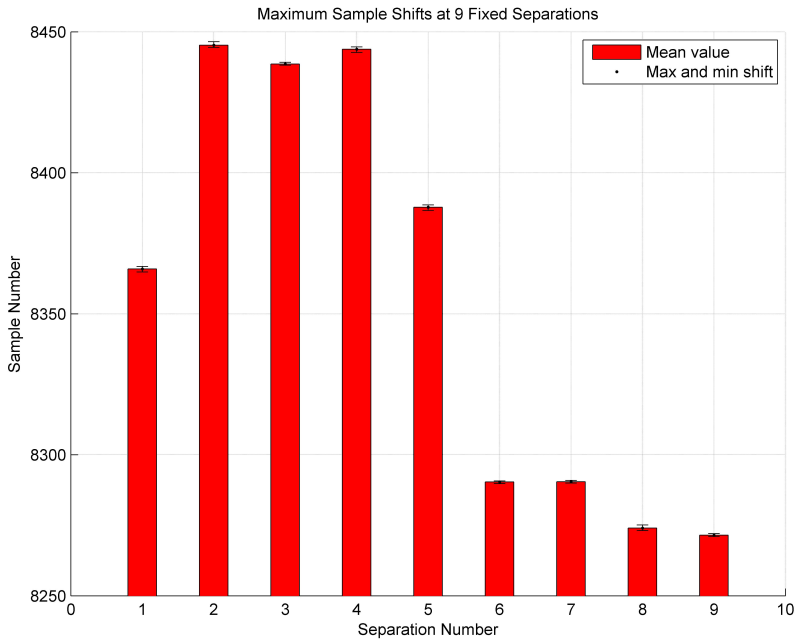

Figure 6-2: DAQ Stability.

The maximum temporal shift in peak location is only 1 sampling interval, corresponding to $20ns$, lower than the alloted $67ns$ time error. For expected SoS around $1500m/s$, final position error due to time sampling would be $30\mu m$.

6.1.2 Radial Positioning Error

Similar to the calibration procedure for ring arrays [28], the radial position error of the transducer is quantified by recording A-scans at 1533 angular positions around a known target ($0.5075in$ ($12.9mm$) diameter nylon 6-6 rod). With a known SoS in the medium, temporal deviations in the first echo peak can be characterized as the radial

position error of the transducer at each angular position. 9 A-scans were collected at each angular position.

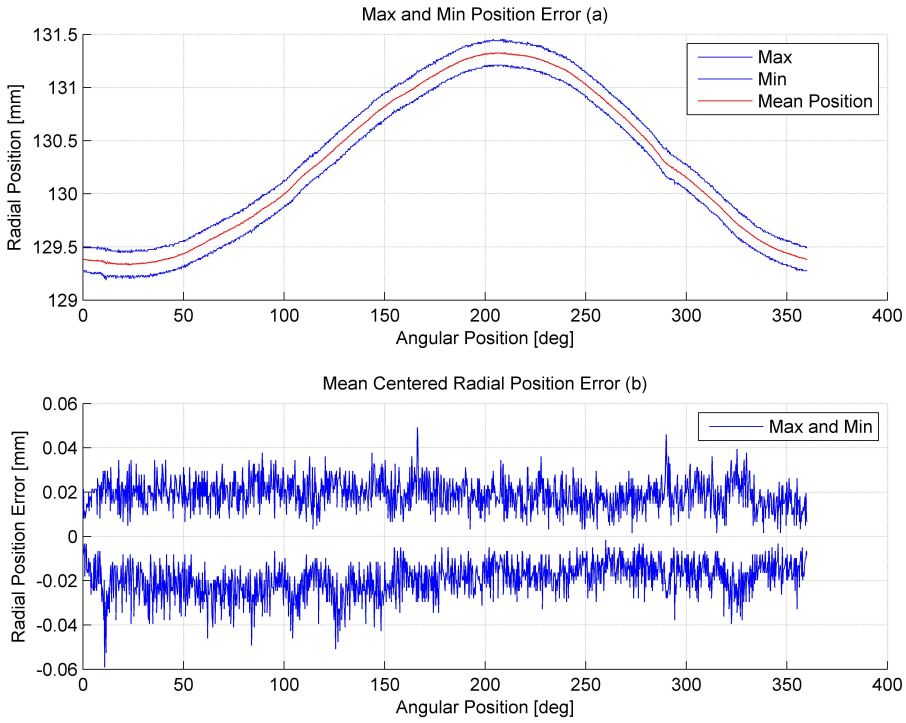

Figure 6-3: Mechanical Positioning Error.

As seen in Fig. 6-3, radial position of the transducer shows $\sim\pm 30\mu m$ deviations at each angular position. Maximum and minimum errors at each position was shifted by $1mm$ to improve clarity (Fig. 6-3 top). The sinusoidal presence in Fig. 6-3 will be discussed in Chapter 7 and is due to the slight non-centered positioning of the nylon rod in the tank. The presented radial error includes the previously evaluated DAQ stability error. However, though inclusive, the total error is still lower than the $50\mu m$ alloted.

6.1.3 Speed of Sound Error

For system characterization in pulse-echo, the SoS is assumed to be global and constant within the imaging volume. Since SoS is temperature dependent and variations are small in deionized water [1], accurate measurement ($\pm 0.1\,^{\circ}\mathrm{C}$) of tempera-

ture can be used to compensate for temperature deviations. Water temperature was measured with a precision thermometer (ThermoWorks-Precision Plus Thermometer) with $\pm 0.05\,^{\circ}\mathrm{C}$ accuracy before each scan.

6.2 Beamwidth Characterization

As discussed in Chapter 5 in Fig. 5-1a, a wide beamwidth transducer is necessary to cover a ROI in the center of the scanning tank. The focused $5MHz$ transducer was simulated in PZFlex to estimate the ROI coverage size in the tank center. As seen in Fig. 6-4, the beam pattern shows a 62° beam width for the focused transducer. At the center of the tank, the ROI covered would be about $\sim 4.9in$ in diameter. This beam width was validated with transmission scans on an empty water tank. A fixed transmitter was pulsed as the receiver scanned around the water tank. The simulated and measured beamwidths are shown in Fig. 6-4 and below.

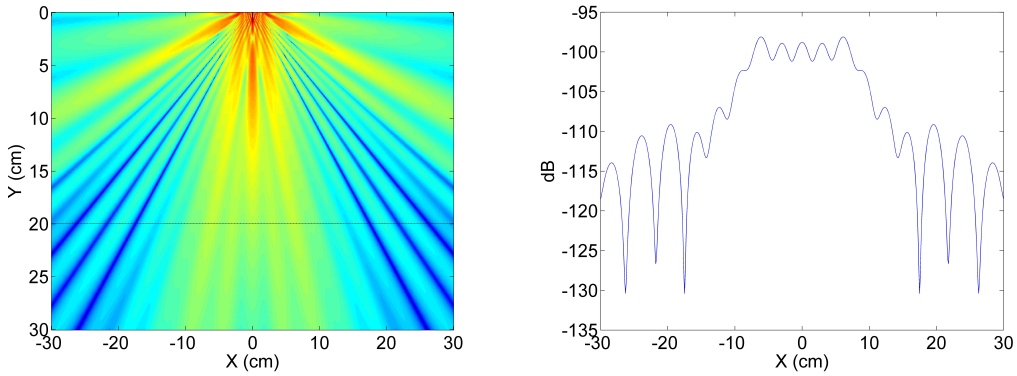

(a) PZFlex Simulation (b) Power profile at $20cm$

Figure 6-4: Simulated transducer beam pattern.

At $20mm$ distance from the face of the transducer (the center of the cylindrical aperture), the simulated beam pattern shows a 62° beamwidth, while the measured beam profile in the empty tank showed 61°. Discrepancies in the power profile can be attributed to the measuring receiver moving in a circular arc while the simulation profile is a linear cut at $20cm$. Overall, the simulation and measurement beamwidth

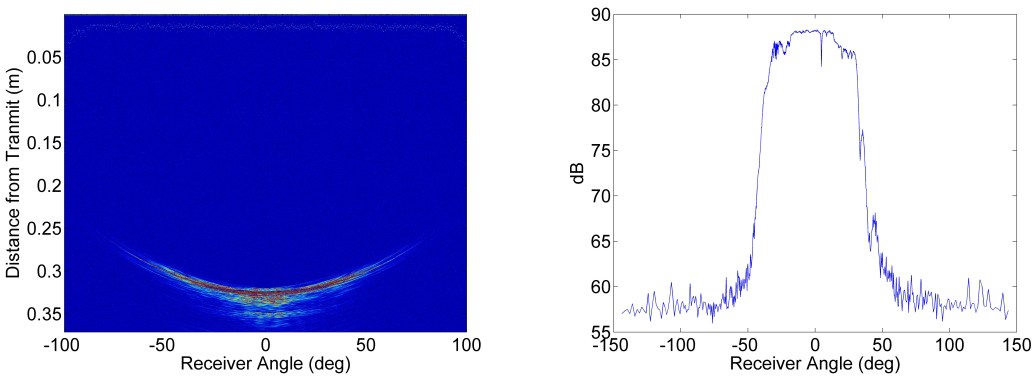

(a) Measured beam pattern

(b) Power profile

Figure 6-5: Measured transducer beam pattern.

show sufficient agreement to validate the transducer beamwidth, corresponding to a $\sim 4.8in$ ROI at the center of the scanning tank.

6.3 Summary

To obtain the best image quality, error sources relevant to accurate localization of scatterers in the tank has been tracked and characterized. The total error budget established from the functional requirements was evaluated against the measured error values. The measured errors were within the defined $50\mu m$ error boundaries. The beamwidth of the focused $5MHz$ transducer was simulated and measured and showed sufficient size to cover a $4.8in$ ROI at the center of the tank.

Chapter 7

Echo Imaging

In this chapter, we present single element pulse-echo image reconstruction of various targets inside the scanning tank. A-scans at each angular position combined to form a cross-sectional B-mode (amplitude scaled brightness) image of the scan target; axial B-mode slices were produced similarly. Image distortions from the receiver angular insensitivity were corrected with a migration algorithm. Raw B-mode and corrected images are both presented in the chapter. Water temperature was measured in the distilled water before each scan to account for deviations in the speed of sound.

7.1 Fixed Height Echo Imaging

Tracing the circular path defined by the ring bearing, the focused $5MHz$ wide beam transducer was used for pulse-echo imaging of various targets at fixed axial heights. A-scans at 1533 angular positions (0.235° angular resolution) with 20000 samples ($50MHz$ sampling rate, 14-bit resolution) were combined to produce B-modes slices of scan targets. B-mode images of two cylindrically symmetric objects, centered in the tank, are shown in Fig. 7-1.

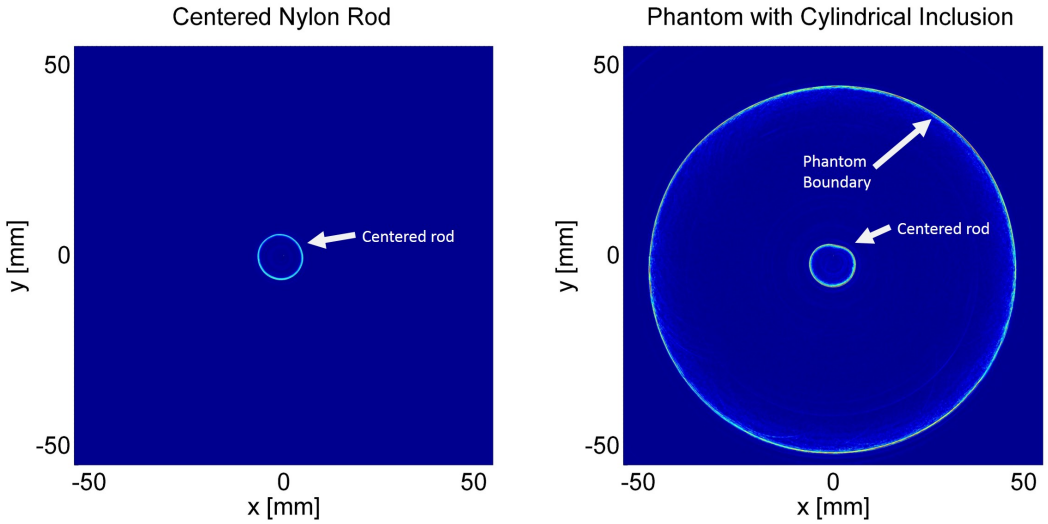

(a) $0.5in$ nylon 6-6 rod (b) Phantom with $0.5in$ nylon rod

Figure 7-1: B-mode images of centered cylindrically symmetric objects

Reflections from the object boundaries are clearly seen. Multilayer propagations through the co-polymer phantom [20] show sufficient echo power to image internal embedded structures.

7.2 Image Distortion

As targets move off-center in tank, reconstructed images show significant distortions in size and shape. As shown in Fig. 7-2, off-center scatterers appear as circular doublets in polar images (Fig. 7-2c and 7-2d) and sinusoids in Cartesian images (Fig. 7-2a and 7-2b). Fig. 7-2b is in grayscale to improve contrast.

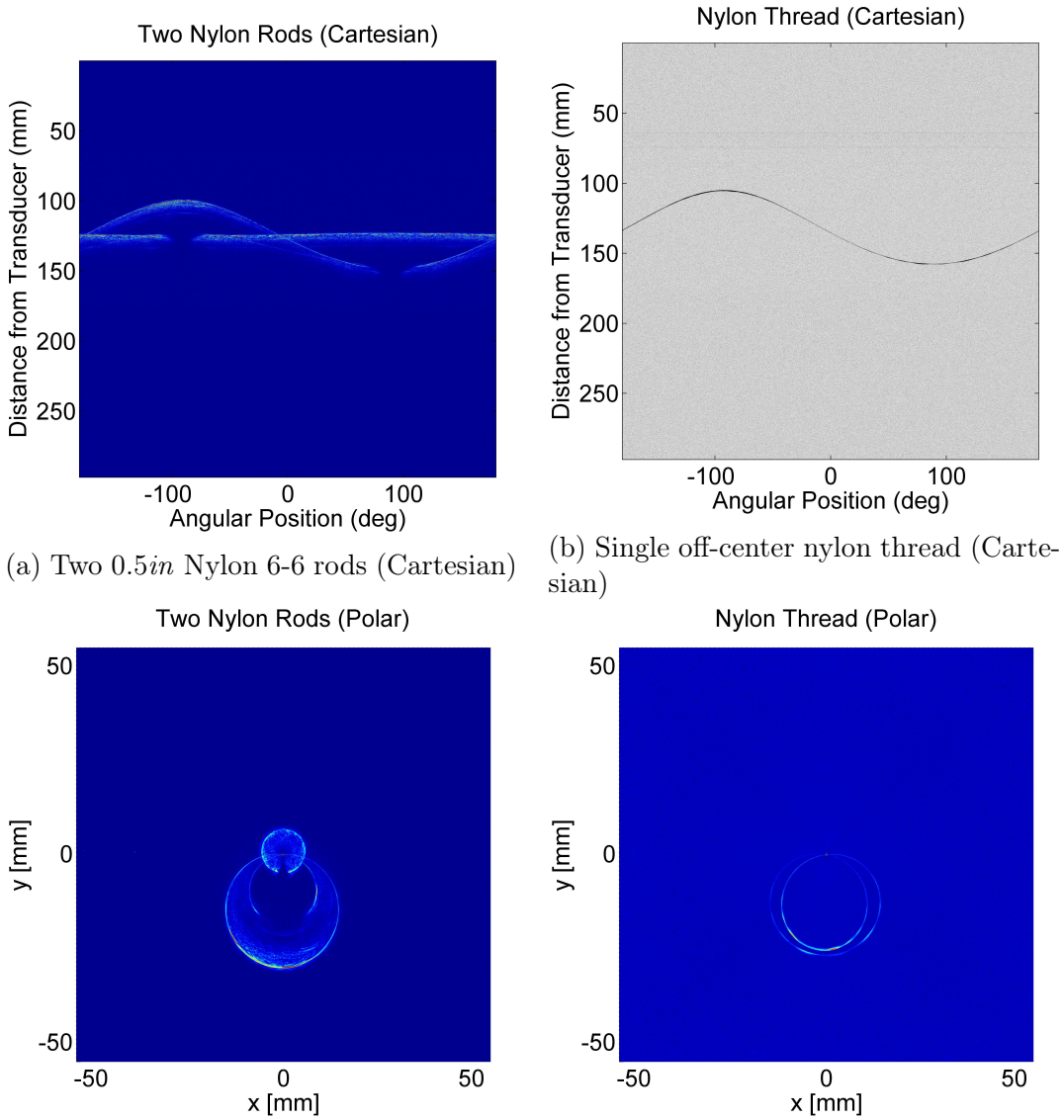

(a) Two $0.5in$ Nylon 6-6 rods (Cartesian)

(b) Single off-center nylon thread (Cartesian)

(c) Two $0.5in$ Nylon 6-6 rods (Polar)

(d) Single off-center nylon thread (Polar)

Figure 7-2: Object distortions in Cartesian and Polar coordinates

The distortions are caused by the wide beamwidth of the transducer. As dis-

cussed in Chapter 6 to cover a ROI, a wide beamwidth is necessary. However, for a focused single element transducer, the receive aperture is directionally insensitive. As discussed by Norton et al. [17], in a circular aperture, each point in a A-scan line actually corresponds to the sum of the echo response from all scatterers along a circular arc centered at the transducer location [17]. This wide beam angular insensitivity creates distortions for off-center scatterers in the tank.

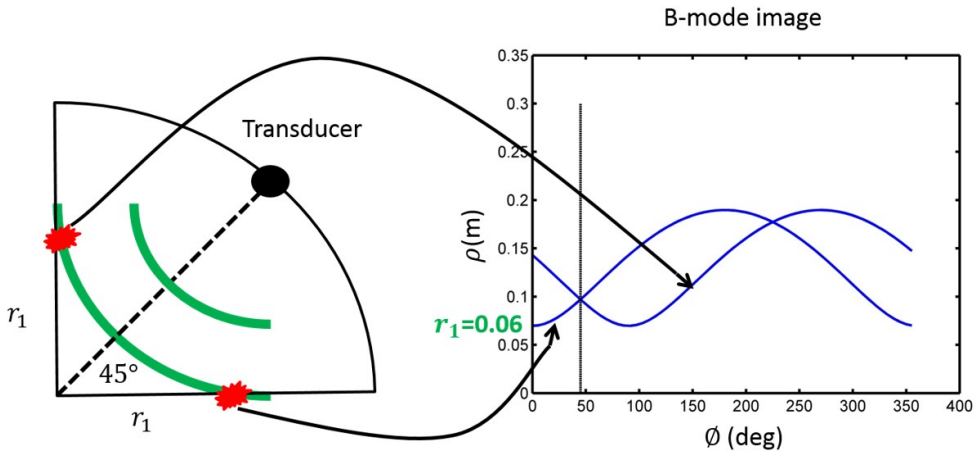

Figure 7-3: Angular Insensitivity of a omni-directional source

As shown in Fig. 7-3, echoes from off angle scatterers will appear directly in-line with the transducer face. However, because the transducer position is known, the expected distorted shape for every point scatterer in the image can be calculated (Eq. 7.1). For example, a point scatterer at θ=0° and r=60mm scanned in 360° pulse-echo with an omni-directional source would produce the (distortion) profile shown in Fig. 7-5d.

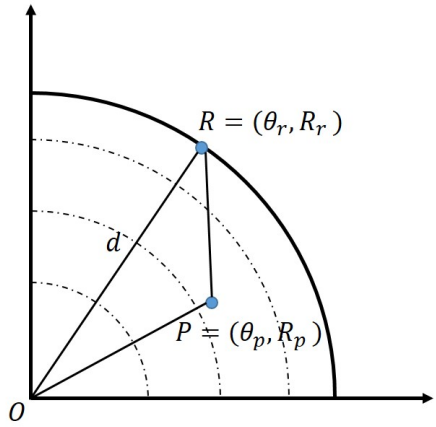

Figure 7-4: Defined transducer (R) and point scatterer (P) coordinates for Eq. 7.1

$$d = \sqrt{(R_r^2 + R_p^2 - 2R_r R_p cos(\theta_r - \theta_p)} \tag{7.1}$$

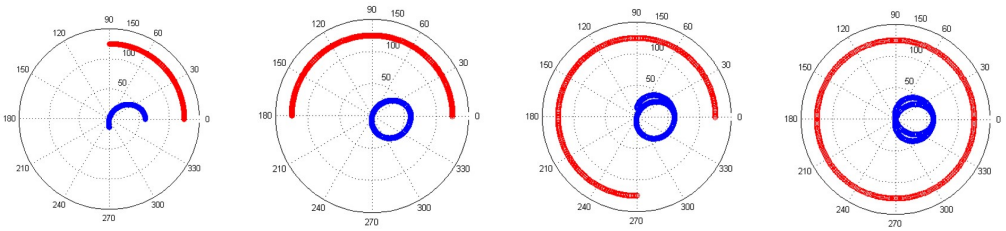

(a) 0-90° (b) 0-180° (c) 0-270° (d) 0-360°

Figure 7-5: Profile of a point scatterer at (0,60mm) viewed in pulse-echo by an omni-directional source/receiver moving in a circular aperture

Since the distortion profile is known for every point inside the scan plane, each distortion profile can be used to sum and migrate echoes for image correction.

7.3 Image Correction Algorithm

From Eq. 7.1, each calculated distortion profile gives the spatial location of the echoes associated with a single point source. In Cartesian coordinates, calculated point scatterer present as sinusoids, in polar coordinates, circular doublets, as shown in Fig. 7-5. This is in agreement with the appearance of the scanned nylon thread (Fig. 7-2d).

For image correction, expected distortion profiles are calculated for every point inside the scan plane. Line integrals along the distortion profiles sum the associated echoes for every point. Summation results from each line integral define the echo strength for each point. This operation can be thought of as accumulating echoes from appropriate A-scans points and moving the summation to the proper location in space. This image correction technique is based on the reflectivity tomography algorithm by Norton [18]. The algorithm is valid for a monostatic setup with an omnidirectional transducer which travels in a circular path and insonifies targets that are weak and omnidirectional scatterers. Flow chart for the image correction algorithm is presented in Fig. 7-6.

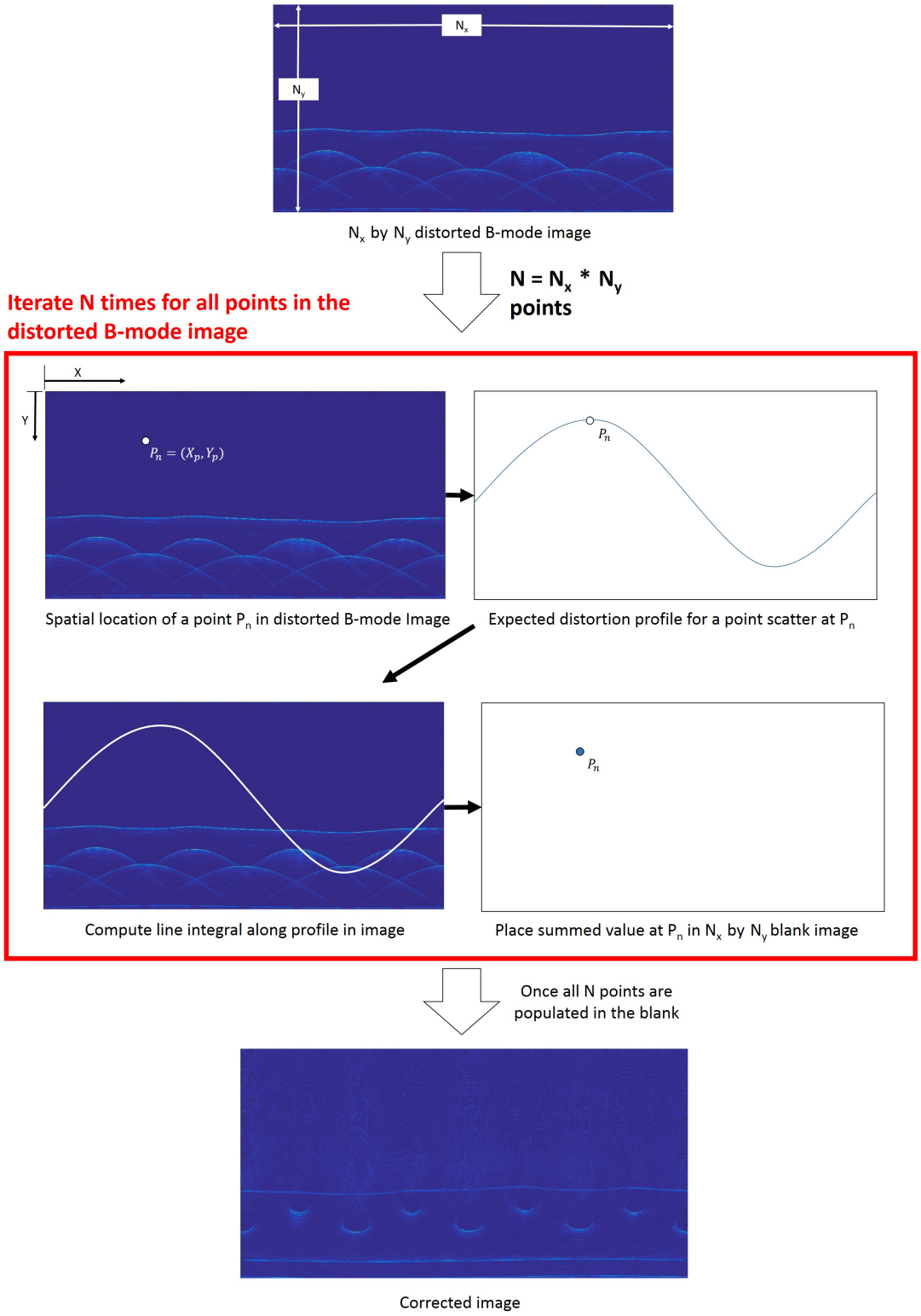

Figure 7-6: Image correction algorithms flow chart

7.3.1 Corrected Images

Corrected B-mode images of the nylon rods and thread are shown in Fig. 7-7.

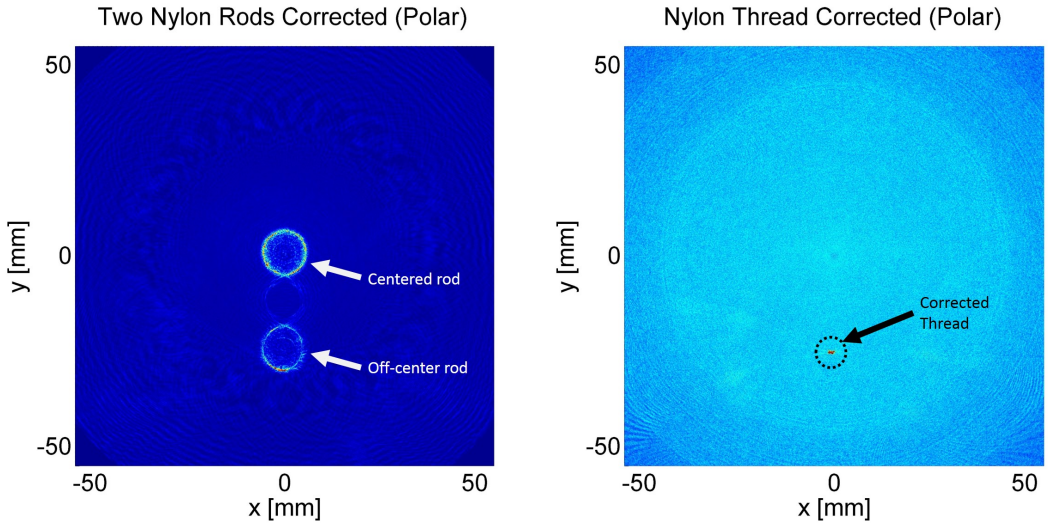

(a) Corrected two nylon rods (b) Corrected off-center nylon thread

Figure 7-7: Correct images after migration

The algorithm correctly recovers the expected shapes and sizes of the scanned targets. Previously distorted nylon rods show with corrected sizes and locations (Fig. 7-7a) and the nylon thread shows as a point scatterer as expected (Fig. 7-7b). However, the algorithm does add noise to the image at the scatterer boundaries. This is a result of the finite axial resolution of the transducer and deviations from the original assumptions of the algorithm.

7.4 Fixed Angle Echo Imaging

In addition to the fixed plane images, A-lines from axial scans were combined to produce axial B-mode slices. Axial pulse-echo scanning is mathematically identical to scanning with a linear array probes. Based the array sampling theory, the maximum sampling resolution should be less than $\lambda/2$ ($150\mu m$ at $5MHz$) to prevent grating lobes in real space [26]. Correspondingly, axial scans used 40 step increments ($127\mu m$) between triggers. Axial scans of the a steel calibration rod and the rod with an added

steel collar is shown in Fig. 7-8. An image of the scan setup is presented in Fig. 7-10.

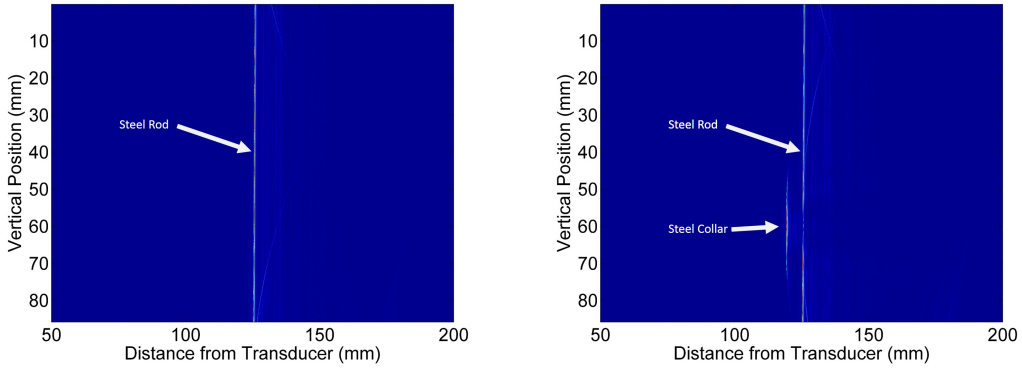

(a) Steel rod (b) Steel rod with collar

Figure 7-8: Vertical steel rod scans

The same image distortion is present in axial scanning as is present in angular scanning. Similar image correction algorithm can be applied in axial scanning with adjustments to the line integrals. In the vertical rectangular plane, the line integral path becomes the Euclidean distance between the transducer and the scatterer, as the transducer is moved.

$$d = \sqrt{(R_r - R_p)^2 + (V_r - V_p)^2} \tag{7.2}$$

Corrected images are shown in Fig. 7-9.

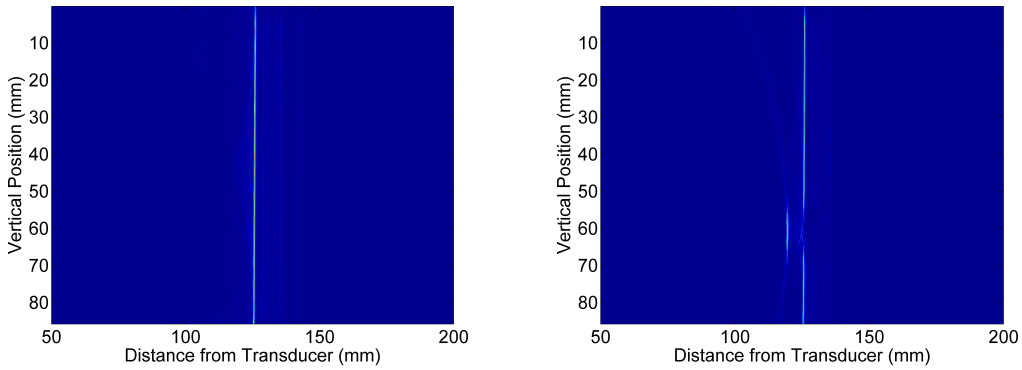

(a) Corrected steel rod (b) Corrected steel rod with collar

Figure 7-9: Corrected vertical steel rod scans

7.4.1 Axial Scan Resolution

Identical to the lateral resolution of linear arrays, the axial scan resolution is defined by the beamwidth of the transducer. With a 61° beamwidth, at the center, the lateral resolution would be $4.8in$. Axial B-mode images show the smearing due to the large axial resolution; two separated steel collars merge into a single body in the axial scans. Steel collars at various separations attached on the steel rod are shown in Fig. 7-11. However, the image correction process improves the lateral resolution and better differentiates the collars at different separations, particularly when comparing Fig. 7-11c and Fig. 7-11d.

The axial scan resolution is critical because it directly affects slice thickness in pulse-echo imaging. Though the image correction algorithm improves the resolution, further improvements can be made by using a non-spherically focused transducer in the future.

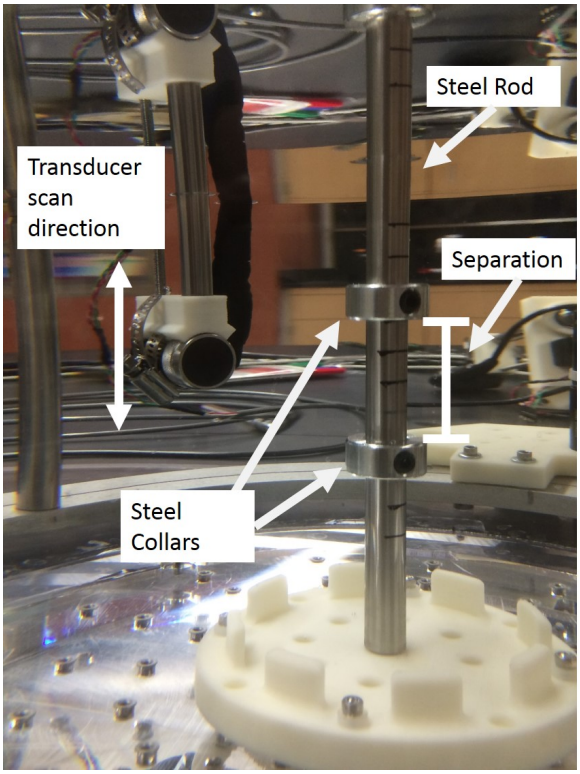

Figure 7-10: Axial scan of steel rod with steel collars.

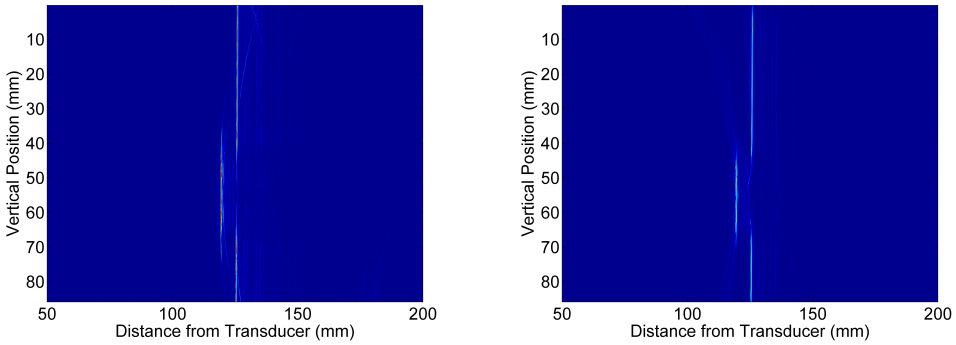

(a) $0mm$ (b) Corrected $0mm$

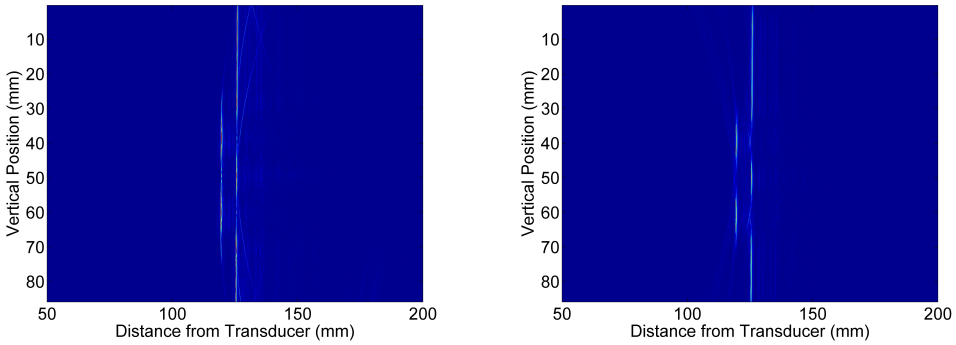

(c) $10mm$ (d) Corrected $10mm$

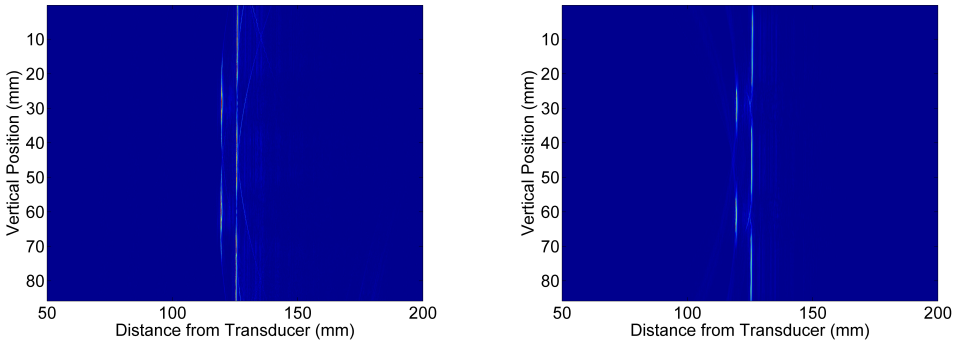

(e) $20mm$ (f) Corrected $20mm$

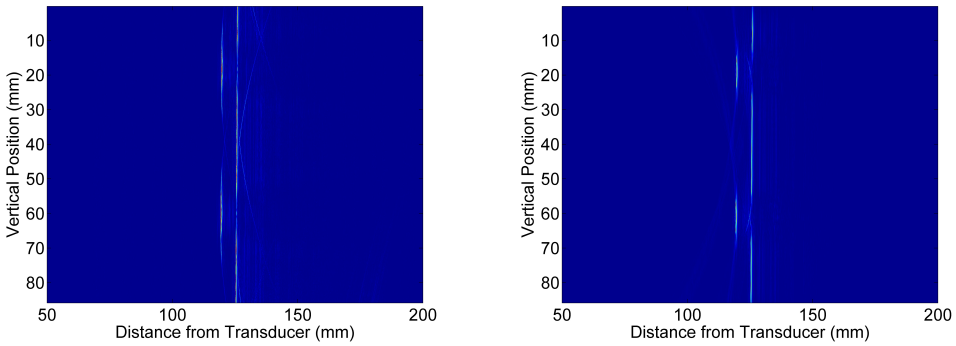

(g) $30mm$ (h) Corrected $30mm$

Figure 7-11: Axial scan of steel collars on a steel rod at various separations

7.5 Bone Scans

Angular and axial B-mode images of a lamb long bone, immersed in the scanning tank, is presented in Fig. 7-15 and Fig. 7-16. Previously discussed angular and axial image corrections were implemented on the images to generate each figure.

The outer bone surfaces are clearly seen along with limited view of the internal structures. Cortical bone thickness can be seen at surfaces directly perpendicular to the transmitted wave. Limited penetration depth due to attenuation of the $5\,MHz$ signal is expected in the bone [14]. With the transducer bandwidth, lower transmitted frequencies ($\sim 500 kHz$) have some penetration into the bone, showing the cortical bone thickness when the incident wave is perpendicular to the bone surface. In future development, lower center frequency transducers should provide better penetration depth into the bone.

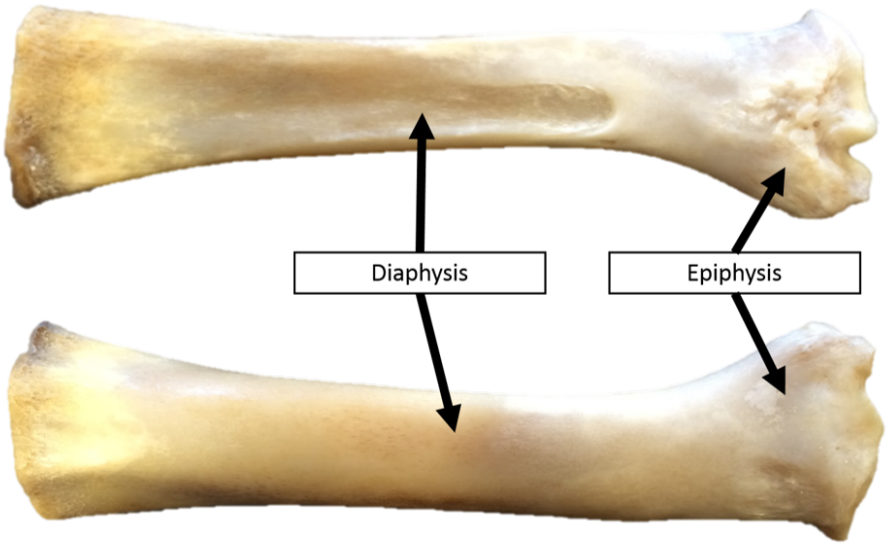

Figure 7-12: Top and bottom view of scanned lamb long bone

Figure 7-13: Lamb long bone at viewed at various angles

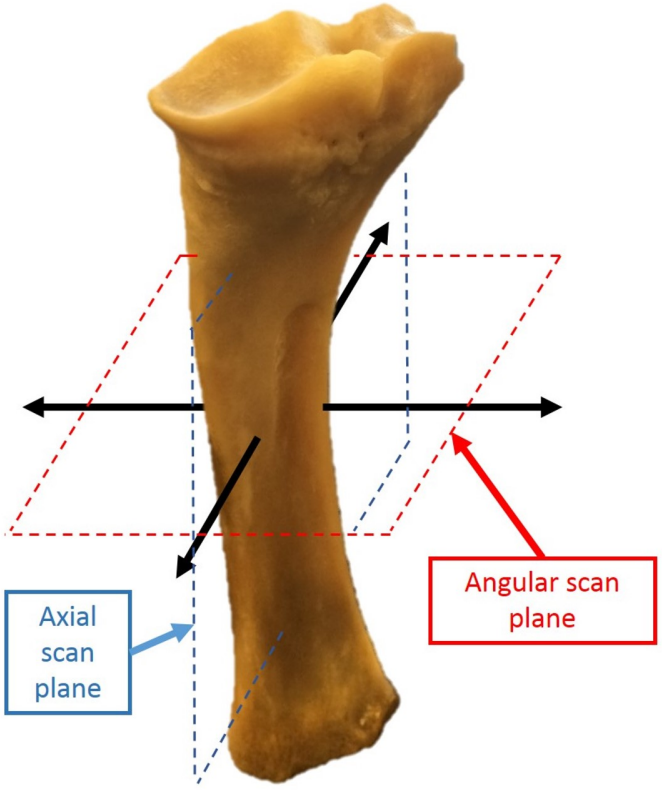

Figure 7-14: Exemplary scan angular and axial scan planes

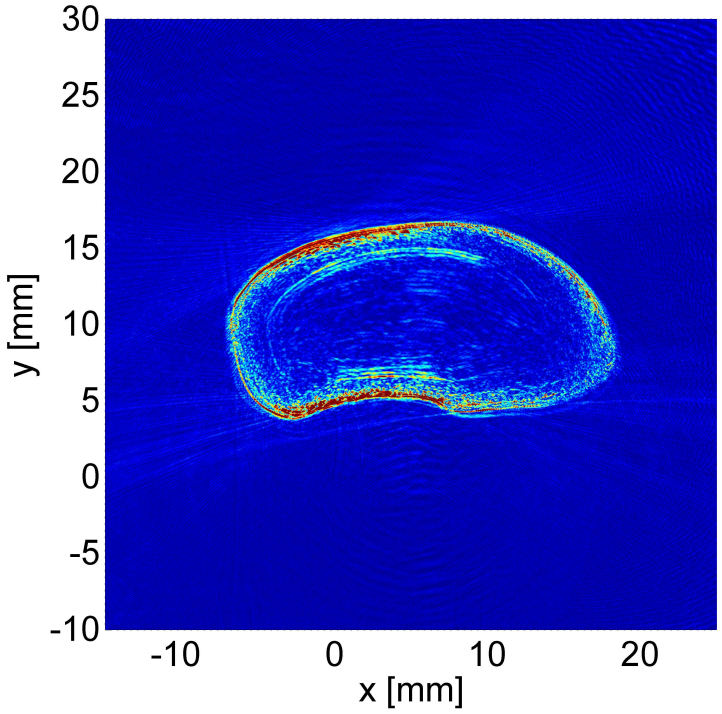

Figure 7-15: Angular scan of a lamb long bone

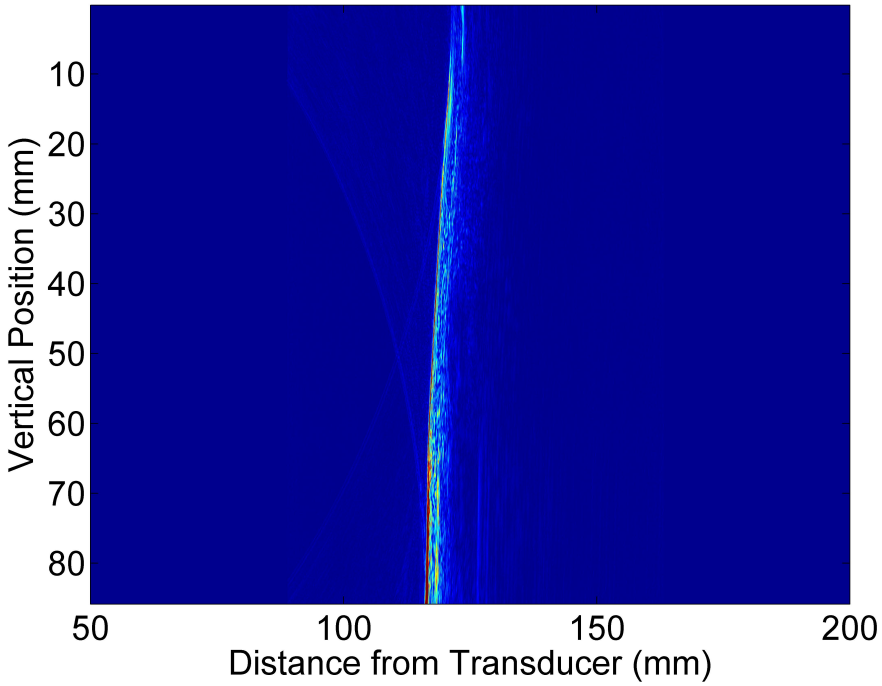

Figure 7-16: Axial scan of a lamb long bone

7.6 Human Forearm

First in-vivo scanning in the system was completed on a human forearms in the scanning tank. Subjects placed their palm flat on the tank base while the transducer scanned circumferentially around the mid forearm. B-mode images before and after image correction are shown in Fig. 7-17 below.

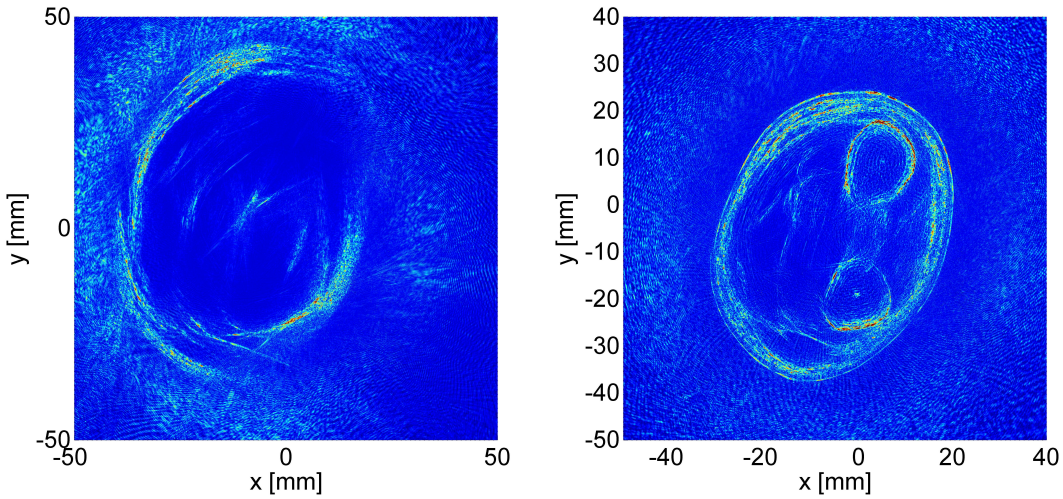

(a) Forearm with motion (b) Forearm with reduced motion

Figure 7-17: Forearm angular scans

In Fig. 7-17b, the skin and bone surfaces are clearly seen after image correction. However, Fig. 7-17a shows severely disconnected structures with or without image correction. This discontinuity is due to movement of the forearm during the scan. This is in agreement with findings from Douglas et al. [4]; involuntary patient movement during ultrasound scanning of lower limbs heavily affect the image quality. Initial imaging of human limbs show promise in capturing the skin and bone surface contours. Additional scan subjects, ground truth comparison with MRI images, and motion compensation algorithms are necessary for further system development.

7.7 Summary

Preliminary echo imaging showed significant image distortion due to the angular insensitivity of the focused single element transducer. Image correction based on the migration technique developed by Norton yielded significantly improved horizontal planar scan and somewhat improved the vertical scan resolution. Image reconstruction has been completed on a lamb bone and has shown penetration into the bone with the wide transducer bandwidth. Cortical bone thickness is visible at particular transducer positions. For in-vivo scanning, a single horizontal B-mode slice of a human forearm has been completed. Results show system sensitivity to scan target movement. In the future, (1) lower frequency transducers will be tested for better penetration into bone, (2) better elevation focused transducers will used to reduce vertical slice thickness, and (3) motion compensation techniques will be explored to account for involuntary patient movement.

Chapter 8

Volumetric Echo Imaging

In this chapter, we combine B-mode cross sections from angular and axial scans to create a volumetric scan of the target. Image correction methods discussed in Chapter 7 are applied in both angular and axial scans respectively.

8.1 Lamb Bone

The same lamb bone scanned in Chapter 7 was scanned at multiple axial positions and multiple angular positions with the focused $5MHz$ transducer. The sliced images sets are shown below in Fig. 8-1 and Fig. 8-2.

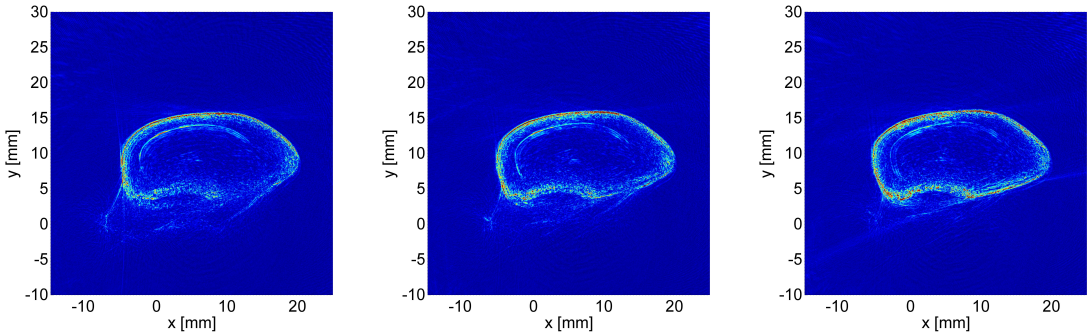

(a) 0 (b) Down $1/8in$ (c) Down $2/8in$

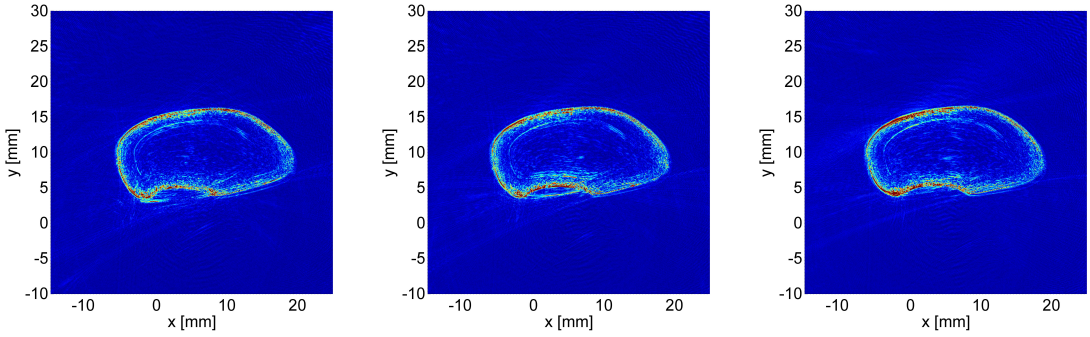

(d) Down $3/8in$ (e) Down $4/8in$ (f) Down $5/8in$

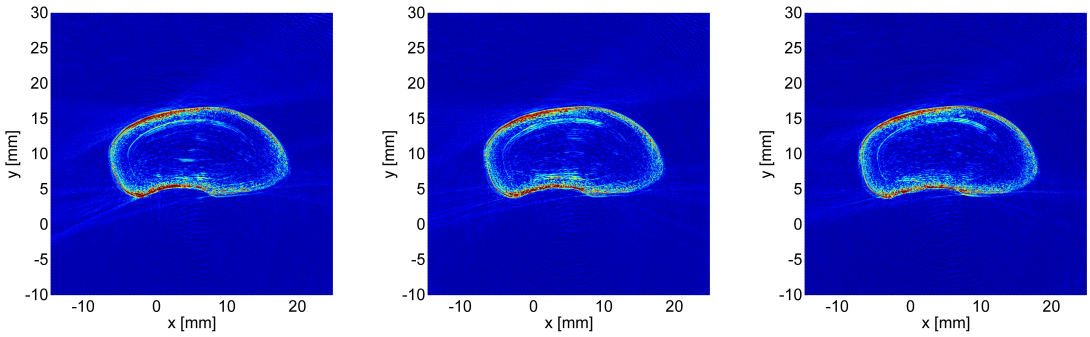

(g) Down $6/8in$ (h) Down $7/8in$ (i) Down $8/8in$

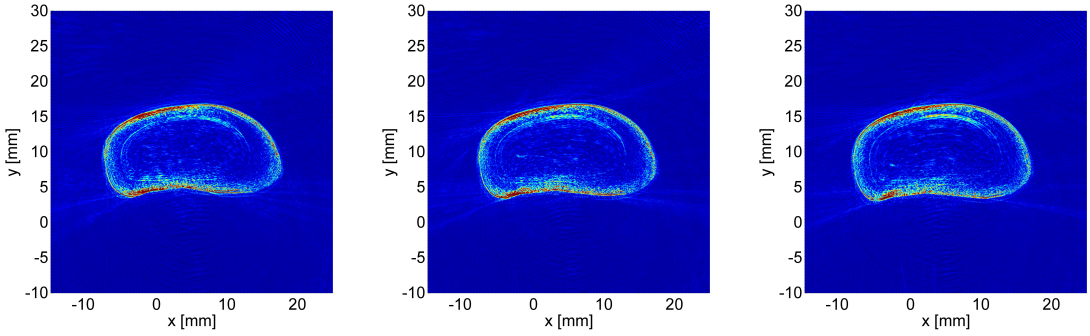

(j) Down $9/8in$ (k) Down $10/8in$ (l) Down $11/8in$

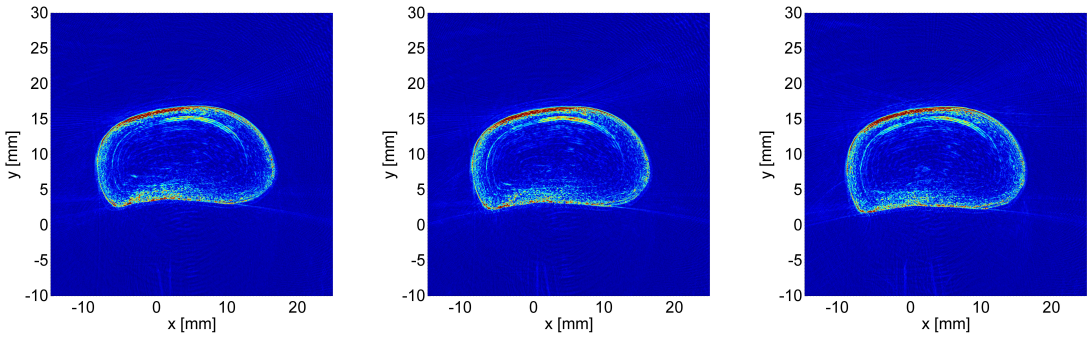

(m) Down 12/8in (n) Down 13/8in (o) Down 14/8in

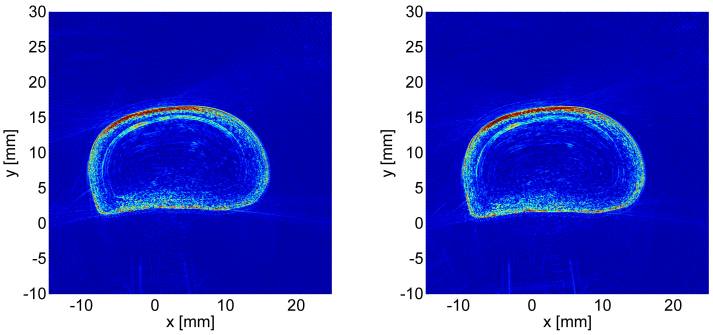

(p) Down 15/8in (q) Down 16/8in

Figure 8-1: Planar scanning of a lamb bone at various heights

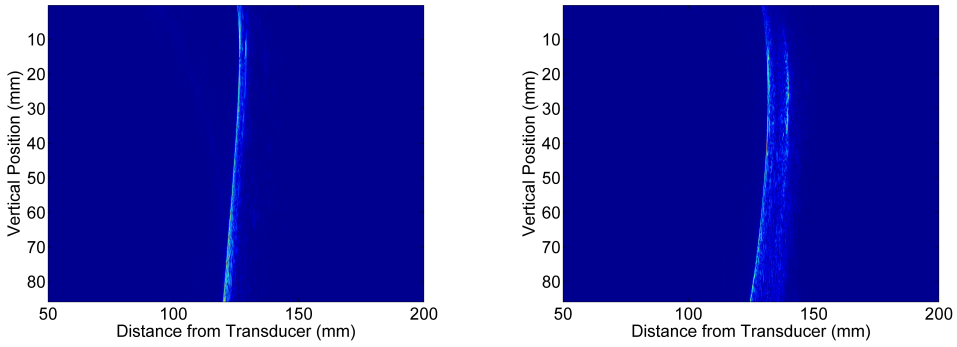

(a) 0°

(b) 45°

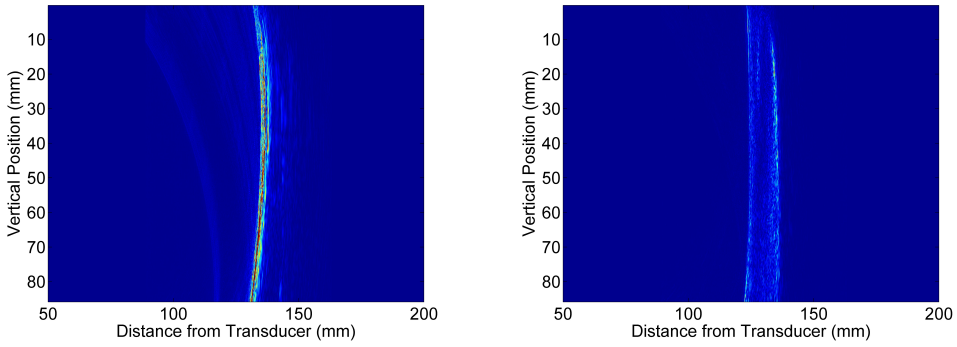

(c) 90°

(d) 135°

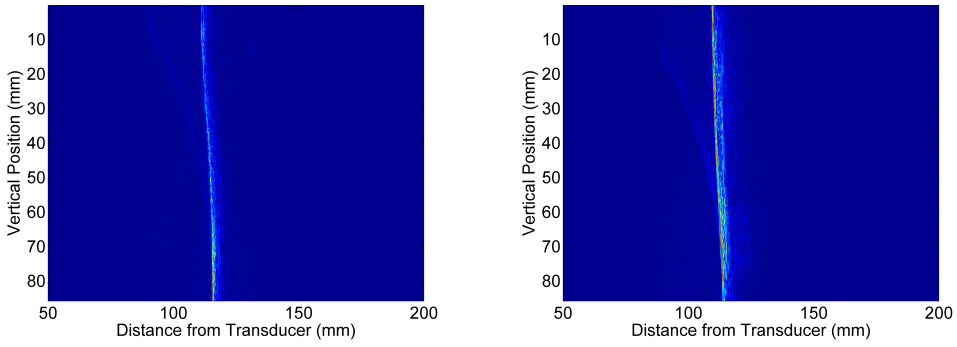

(e) 180°

(f) 225°

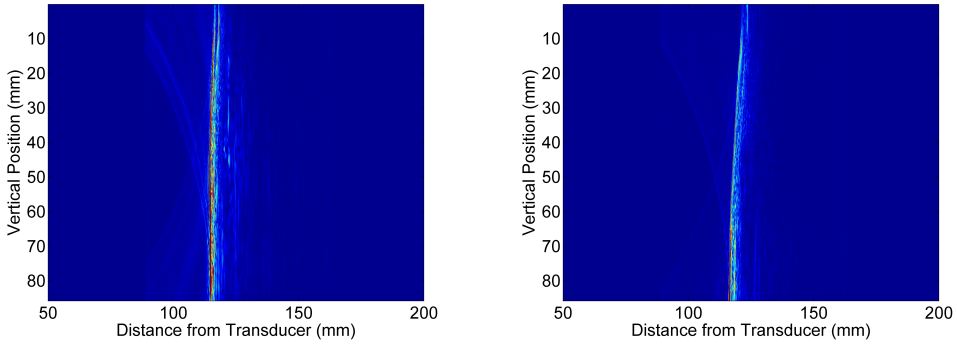

(g) 270°

(h) 315°

Figure 8-2: Axial scanning of a lamb bone at various fixed angular positions

In general, the bone diaphysis (Fig. 8-1h to 8-1m) shows the clearest cross sectional images. Due to the wide beamwidth, the bottom fixturing and the bone epiphysis creates artifacts when the transducer is at maximum or minimum axial positions. Improving the elevation focusing of the transducer (reducing the slice thickness) will help remove these artifacts.

In both axial and angular scans, the outer bone boundary can be seen. Segmentation of the bone surface can provide valuable boundary information for finite element (FE) modeling for improving prosthetic fittings [9]. However, as expected, the $5\,MHz$ center frequency does have limited transmission into the bone. Low frequency bands show some penetration into the bone when the incident wave is perpendicular to the bone surface. Cortical bone thickness can be estimated but is not fully reliable since the speed of sound (SOS) differences inside the bone are not factored into the image. To account for SOS differences, initial tomographic SOS mapping can be added to correct pulse-echo images [5] [11]. Though limited, transmitted signals into the bone demonstrates the $5\,MHz$ transducer's wide bandwidth to generate low frequency signals. This is encouraging as it enables us to use the same transducers for tomographic imaging of a limb section.

Chapter 9

Tomography

Discussed in both Chapter 7 and Chapter 8, tomographic scanning of the imaging volume accounting for speed of sound (SoS) and attenuation variations can work to improve ultrasound image accuracy and image quality. Inverse methods including ray tracing and full wave inversions can map the SoS and attenuation distributions to compound back into the original B-mode image [22] . In this chapter we discuss preliminary work with ray trace inversions and preliminary work with tomographic scans.

9.1 Ray Tracing

In ray-based methods, transmitted waves are approximated to travel on straight paths, or rays, through the medium. Spatial variations in the SoS in an inhomogeneous medium will cause variations in the travel time between each transmit and receive pairs, when compared to a homogeneous medium with a constant SoS. The image plane is discretized into a vector-matrix with an associated guess of the SoS at each point. An iterative inversion scheme then minimized the discrepancy between the measured time of flight for each ray versus the computed time of flight for each ray on the SoS vector-matrix [21]. Additional weights and constraints can be added in the inversion to enforce smoothness in the reconstructed SoS map.

More complex ray tracing methods such as bent-ray inversions improve upon the

straight-ray method by accounting for the bending of the ray paths in an inhomogeneous medium based on Fermat's Principle and Snell's Law [15]. Bent-ray inversions method has shown improved lesion sharpness when imaging breast tissues [15]. General accuracy of the SoS map from ray tracing methods is constrained by the number of intersecting rays at each point in the vector-matrix. Sufficient rays and corresponding observations must be made to correctly recreate the SoS map [28].

9.1.1 Inversions on Simulated Data

To develop, validate, and improve algorithms, preliminary ray-trace inversions were tested on simulated sound speed data (in collaboration with Jon Fincke). A known sound speed map (Fig. 9-1a) was defined and 13,708 travel time observations were made around the boundary to enable simulated transmission scanning. Bent-ray inversion of the simulated travel times produced the sound speed map shown in Fig. 9-1.

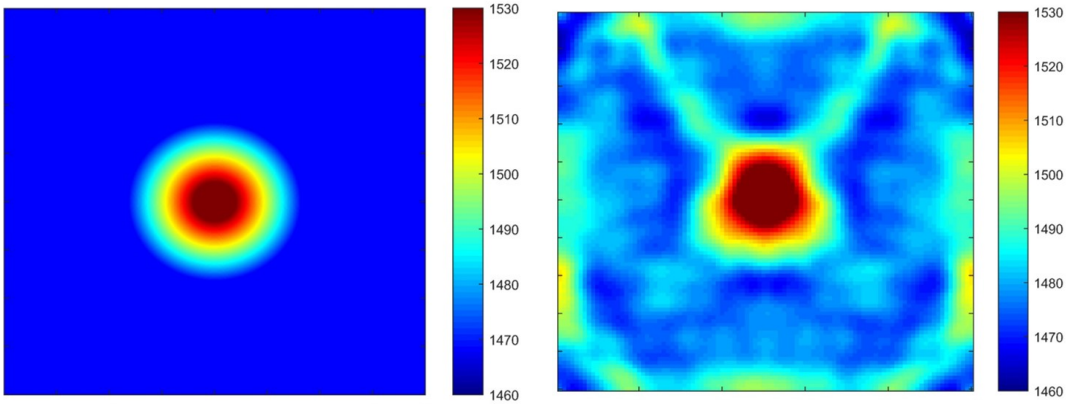

(a) SoS map (b) Reconstructed SoS map

Figure 9-1: Ray tracing SoS reconstruction

Preliminary SoS mapping show agreement between the actual and reconstructed sound speed maps at the center. Additional improvements can be made to reduce artifacts. Further testing of the algorithm on more complex sound speed maps and actual scan data is currently in progress.

9.1.2 Tomography Scans

Two tomographic scans (pig leg, co-polymer phantom) have been completed on the physical system to enable testing of various tomographic reconstruction algorithms. Full tomographic scans composed of: 74 transmit locations at 5° increments around the target, 180° (pig leg) or 330° (phantom) receive sweeps centered opposite each transmit locations at 0.235° (pig leg) and 2.29° (phantom) increments, respectively. Each scan, in total, produced more than $2\,GB$ of data and took over $1hr$ to complete. This long scan time can be significantly reduced by adding addition receivers and improving the mechanical setup to avoid wire wrapping during continuous receiver rotations. Tomographic imaging of a pig limb section is shown in Fig. 9-2. The limb section is bagged in an ultrasound sleeve to prevent contamination of the transducers.

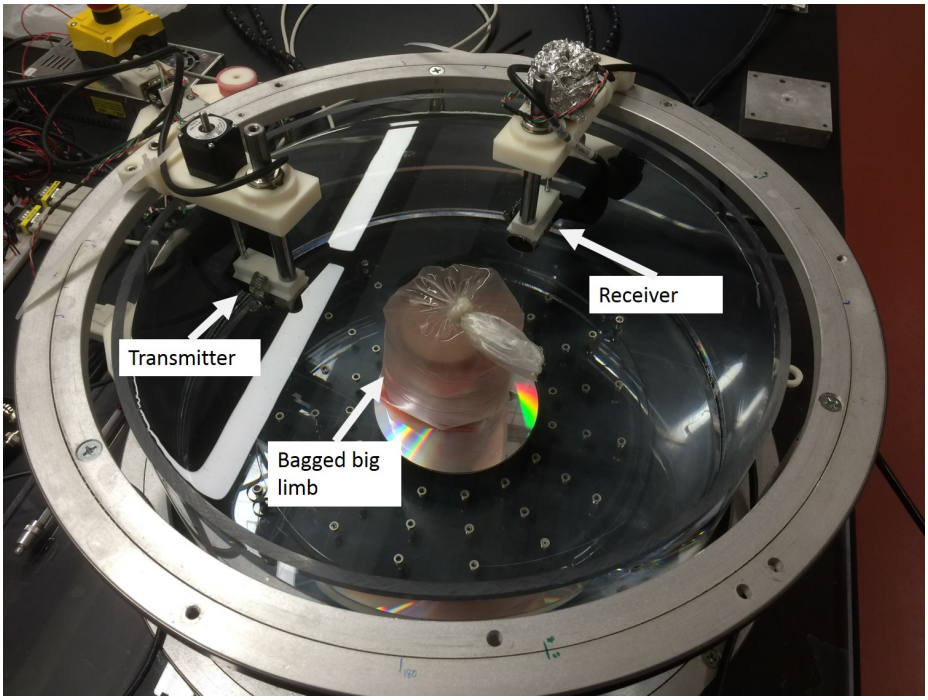

Figure 9-2: Tomographic imaging of a pig limb section

9.1.3 Signal Transmission

To ensure transmission through the pig leg, B-mode images of the received waves at a single transmit location is shown in Fig 9-3.

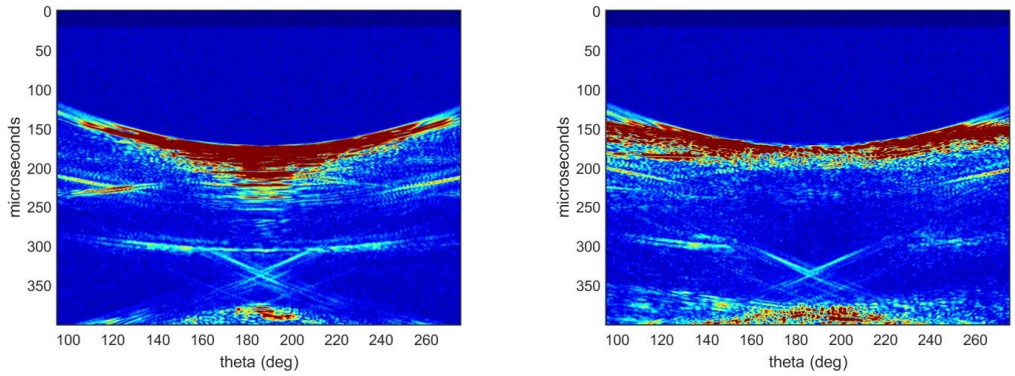

(a) Transmission B-mode in empty tank (b) Transmission B-mode with pig leg

Figure 9-3: Transmission B-mode images

As seen in Fig. 9-3b, the transmitted wave penetrated the pig limb to reach the receiver on the opposite side. Receiving transmission through the pig bone is encouraging since it enables testing of the ray trace inversion on bone. To find the frequencies bands that transmitted through bone, a spectrogram of the received waves was computed (Fig. 9-4)

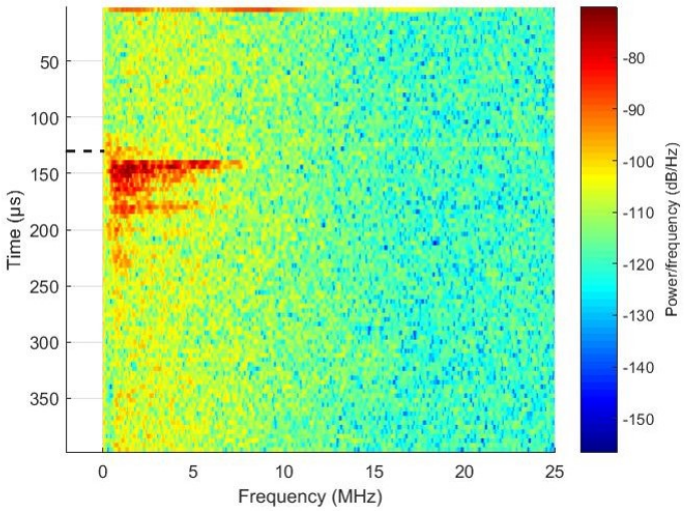

Figure 9-4: Spectrogram of received signals

The spectrogram showed that the $500kHz$ band was the first to arrive through bone. Higher frequencies arrived with delays. This advises using lower frequencies for better through bone transmission, in agreement with previous reports [13].

9.2 Summary

A preliminary ray trace algorithm has been developed and tested on simulated data. Reconstructions show promising agreement between the actual and reconstructed SoS maps. Tomographic scans have been completed on physical objects in the scanner and is ready for reconstruction with ray tracing or other tomographic techniques.

Chapter 10

Conclusion

10.1 Summary

A single element 3D UST system has been designed and built to support iterative development of algorithms targeting (1) improving prosthetic fittings, (2) monitoring bone density deterioration, and (3) quantifying neuromuscular disease progression. The designed system is capable of scanning targets in either pulse-echo or transmission modes. The system consists of two independently moving single element transducers enclosing a cylindrical aperture around the scan target. High resolution position control of these transducers enables precise alignment of transmit and receive pairs within the scan volume.

This thesis presents the mechanical design, software design, system characterization, and preliminary pulse-echo/tranmission imaging of the single element 3D ultrasound system. The mechanical system has shown sufficient accuracy and flexibility to enable testing of various scanning algorithms and transducers. Initial echo images show promise in detection of skin and bone boundaries within the scan volume. Tomographic scans have been completed and initial ray tracing algorithms have been developed.

10.2 Future Work

Mechanically, the system can be improved by better cabling, geared bearings, and kinematic couplings. Power and signal cables between moving and non-moving components limits the number of bearing rotations before cable twisting or entanglements. In addition, the encoding tape attached on the outer races of the bearings each have a notch where the tape ends meet. Since no quadrature signal is received within the notch, crossing this notch with the encoder readhead causes a shift in the angular positioning. The absolute angle subtended by the notch must be measured and added or subtracted for any rotations crossing the notch. In future designs, low-noise slip rings could eliminate the rotation limitations and geared ring bearings could eliminate the notch completely by moving angular encoding directly to the motor. Lastly, kinematic couplings on the transducer holders could more repeatably positioning the transducers during attachment.

Based on the literature [21] [22] [15], compounding tomographic and back scatter information for image reconstruction can sharply increases the image accuracy and image quality in soft tissue imaging. For the targeted applications, more sophisticated echo and transmission algorithms will be developed, accommodating strong directional scattering and complex propagation of sound in soft tissue with bone. The tomographic scanning time will be shortened by implementing smarter sampling algorithms [25] or attaching additional receive transducers to reduce the receiver sweep arc. Data quantity can be reduced by adding FPGA on the receive channels to demodulate data. Image reconstruction time can also be reduced by using GPU clusters for processing [2] Transducer with better elevation focusing and lower center frequency will be tested in the system to reduce the slice thickness and improve transmission through bone.

Bibliography

[1] Nykolai Bilaniuk and George S. K. Wong. Speed of sound in pure water as a function of temperature. *The Journal of the Acoustical Society of America*, 93(3):1609–1612, March 1993.

[2] Matthias Birk, Michael Zapf, Matthias Balzer, Nicole Ruiter, and JÃijrgen Becker. A comprehensive comparison of GPU- and FPGA-based acceleration of reflection image reconstruction for 3d ultrasound computer tomography. *J Real-Time Image Proc*, 9(1):159–170, September 2012.

[3] Katharine Bushby, Richard Finkel, David J. Birnkrant, Laura E. Case, Paula R. Clemens, Linda Cripe, Ajay Kaul, Kathi Kinnett, Craig McDonald, Shree Pandya, James Poysky, Frederic Shapiro, Jean Tomezsko, Carolyn Constantin, and DMD Care Considerations Working Group. Diagnosis and management of Duchenne muscular dystrophy, part 1: diagnosis, and pharmacological and psychosocial management. *The Lancet. Neurology*, 9(1):77–93, January 2010.

[4] T. Douglas, S. Solomonidis, W. Sandham, and W. Spence. Ultrasound imaging in lower limb prosthetics. *IEEE Transactions on Neural Systems and Rehabilitation Engineering*, 10(1):11–21, March 2002.

[5] Nebojsa Duric, Peter Littrup, Lou Poulo, Alex Babkin, Roman Pevzner, Earle Holsapple, Olsi Rama, and Carri Glide. Detection of breast cancer with ultrasound tomography: first results with the Computed Ultrasound Risk Evaluation (CURE) prototype. *Med Phys*, 34(2):773–785, February 2007.

[6] Paul L. Enright. The Six-Minute Walk Test. *Respir Care*, 48(8):783–785, August 2003.

[7] Mikko A. Hakulinen, Judd S. Day, Juha TÃűyrÃďs, Matti Timonen, Heikki KrÃűger, Harrie Weinans, Ilkka Kiviranta, and Jukka S. Jurvelin. Prediction of density and mechanical properties of human trabecular bone in vitro by using ultrasound transmission and backscattering measurements at 0.2-6.7 MHz frequency range. *Physics in Medicine and Biology*, 50(8):1629–1642, April 2005.

[8] C. Hansen, A. Schasse, N. Huttebrauker, M. Ashfaq, W. Wilkening, and Helmut Ermert. 9c-2 Reconstruction of Speed of Sound for a Correction of Transit Time in Full Angle Spatial Compounding. In *IEEE Ultrasonics Symposium, 2007*, pages 785–788, October 2007.

[9] Ping He, Kefu Xue, Yu Fan, and Yiwei Wang. Test of a vertical scan mode in 3-D imaging of residual limbs using ultrasound. *Journal of Rehabilitation Research & Development*, 36(2), 1999.

[10] M. Hollenhorst, C. Hansen, N. HÃijttebrÃď uker, A. Schasse, L. Heuser, H. Ermert, and G. Schulte-Altedorneburg. Ultrasound Computed Tomography in Breast Imaging: First Clinical Results of a Custom-Made Scanner. *Ultraschall in der Medizin - European Journal of Ultrasound*, 31(06):604–609, December 2010.

[11] Torsten Hopp, Lukas Åăroba, Michael Zapf, Robin Dapp, Ernst Kretzek, Hartmut Gemmeke, and Nicole V. Ruiter. Breast Imaging with 3d Ultrasound Computer Tomography: Results of a First In-vivo Study in Comparison to MRI Images. In Hiroshi Fujita, Takeshi Hara, and Chisako Muramatsu, editors, *Breast Imaging*, number 8539 in Lecture Notes in Computer Science, pages 72–79. Springer International Publishing, June 2014.

[12] G. T. ANAST I M SIEGEL. The determination of fracture healing by measurement of sound velocity across the fracture site. *Surgery, gynecology & obstetrics*, 107(3):327–32, 1958.

[13] C. M. Langton, S. B. Palmer, and R. W. Porter. The measurement of broadband ultrasonic attenuation in cancellous bone. *Engineering in medicine*, 13(2):89–91, 1984.

[14] Pascal Laugier and Guillaume HaÃŕat. *Bone Quantitative Ultrasound*. Springer Science & Business Media, November 2010.

[15] Cuiping Li, Nebojsa Duric, Peter Littrup, and Lianjie Huang. In vivo breast sound-speed imaging with ultrasound tomography. *Ultrasound in Medicine & Biology*, 35(10):1615–1628, October 2009.

[16] A. F. Mak, M. Zhang, and D. A. Boone. State-of-the-art research in lower-limb prosthetic biomechanics-socket interface: a review. *Journal of Rehabilitation Research and Development*, 38(2):161–174, April 2001.

[17] Stephen J. Norton. Reconstruction of a two-dimensional reflecting medium over a circular domain: Exact solution. *The Journal of the Acoustical Society of America*, 67(4):1266–1273, 1980.

[18] Stephen J. Norton and Melvin Linzer. Ultrasonic reflectivity imaging in three dimensions: Reconstruction with spherical transducer arrays. *Ultrasonic Imaging*, 1(3):210–231, July 1979.

[19] Office of the Surgeon General (US). *Bone Health and Osteoporosis: A Report of the Surgeon General*. Reports of the Surgeon General. Office of the Surgeon General (US), Rockville (MD), 2004.

[20] J. Oudry, C. Bastard, V. Miette, R. Willinger, and L. Sandrin. Copolymer-in-oil Phantom Materials for Elastography. *Ultrasound in Medicine & Biology*, 35(7):1185–1197, July 2009.

[21] Neslihan Ozmen, Robin Dapp, Michael Zapf, Hartmut Gemmeke, Nicole V. Ruiter, and Koen W. A. van Dongen. Comparing different ultrasound imaging methods for breast cancer detection. *IEEE transactions on ultrasonics, ferroelectrics, and frequency control*, 62(4):637–646, April 2015.

[22] Bryan Ranger, Peter Littrup, Neb Duric, Cuiping Li, Steven Schmidt, Jessica Lupinacci, Lukasz Myc, Amy Szczepanski, Olsi Rama, and Lisa Bey-Knight. Breast imaging with ultrasound tomography: A comparative study with MRI. In *SPIE Medical Imaging*, pages 762906–762906. International Society for Optics and Photonics, 2010.

[23] Nicole V. Ruiter, Michael Zapf, Torsten Hopp, and Hartmut Gemmeke. Experimental evaluation of noise generated by grating lobes for a sparse 3d ultrasound computer tomography system. volume 8675, pages 86750N–86750N–8, 2013.

[24] H. Schomberg. An improved approach to reconstructive ultrasound tomography. *Journal of Physics D: Applied Physics*, 11(15):L181, October 1978.

[25] R. Sloun, A. Pandharipande, M. Mischi, and L. Demi. Compressed Sensing for Ultrasound Computed Tomography. *IEEE Transactions on Biomedical Engineering*, PP(99):1–1, 2015.

[26] Thomas L. Szabo. *Diagnostic Ultrasound Imaging: Inside Out, Second Edition*. Academic Press, Amsterdam ; Boston, 2 edition edition, December 2013.

[27] A. K. Topper and G. R. Fernie. Computer-aided design and computer-aided manufacturing (CAD/CAM) in prosthetics. *Clinical Orthopaedics and Related Research*, (256):39–43, July 1990.

[28] R.C. Waag and R.J. Fedewa. A Ring Transducer System for Medical. *IEEE Transactions on Ultrasonics, Ferroelectrics, and Frequency Control*, 53(10):1707–1718, October 2006.